ИНСТИТУТ ЗА ФИЗИКУ

ПРИМЉЕНО: 12. 09. 2024			
Рад.јед.	б р о ј	Арх.шифра	Прилог
0801	1627/1		

Научном већу Института за физику у Београду

Београд, 05.09.2024.

Предмет:

Молба за покретање поступка за стицање звања истраживач-сарадник

На основу испуњености услова предвиђених Правилником о стицању истраживачких и научних звања, прописаног од стране ресорног Министарства, молим Научно веће Института за физику у Београду да покрене поступак за мој избор у звање истраживач сарадник.

У прилогу достављам:

1. Мишљење руководиоца лабораторије са предлогом комисије за избор у звање
2. Стручну биографију
3. Преглед научне активности
4. Списак научних радова
5. Потврду о статусу студента докторских студија и пријављеној теми докторске дисертације
6. Копије диплома основних и мастер студија
7. Копије научних радова

С поштовањем,

Марта Букумира

Истраживач приправник

ПРИМЉЕНО: 12. 09. 2024

Рад.јед.	б р о ј	Арх.шифра	Прилог
0801	1627/2		

НАУЧНОМ ВЕЋУ ИНСТИТУТА ЗА ФИЗИКУ У БЕОГРАДУ

Предмет: Мишљење руководиоца лабораторије о избору Марте Букумире у звање истраживач сарадник

Марта Букумира, мастер физичар, је запослена у Лабораторији за биофизику у оквиру Центра за фотонику. Студнет је докторских студија из Биофизике при Универзитету у Београду. Докторску дисертацију из области нелинеарне ласерске скенирајуће микроскопије ради под руководством др Наташе Тодоровић, вишег научног сарадника запослене у Институту за биолошка истраживања „Синиша Станковић“ у Београду и др Александра Крмпота, научног саветника запосленог у Институту за физику у Београду.

С обзиром да испуњава предвиђене услове прописане Законом о науци и истраживањима и Правилником о стицању научних и истраживачких звања Министарства науке, технолошког развоја и иновација, те сам сагласан да Научно веће Института за физику у Београду покрене поступак за избор Марте Букумире у звање истраживач сарадник.

Предлажем да комисију за избор Марте Букумире у звање истраживач сарадник чине:

1. др Александар Крмпот, научни саветник, Институт за физику у Београду
2. др Наташа Тодоровић, виши научни сарадник, Институт за биолошка истраживања „Синиша Станковић“ у Београду, и
3. др Михаило Рабасовић, виши научни сарадник, Институт за физику у Београду.

У Београду,
12. IX 2024.

Руководилац лабораторије,

др Александар Крмпот
научни саветник
Институт за физику

Кратка биографија

Марта Букумира рођена је 22. марта 1996. године у Краљеву. Завршила је Основну школу „Димитрије Туцовић“ 2011. године и наставила образовање у Гимназији Краљево, природно-математички смер, где је 2015. добила диплому „Вук Караџић“ за изузетан успех и примерно владање. Уписала се на Физички факултет Универзитета у Београду 2015. године, смер Примењена и компјутерска физика, Метролошки модул. Током основних студија стекла је практично искуство кроз праксу у Лабораторији за метрологију и еталонирање на факултету. Дипломирала је 2019. године са просечном оценом 9.72/10.0. Исте године започиње мастер студије на Физичком факултету, смер Теоријска и експериментална физика. Мастер диплому је стекла 2021. године, са просечном оценом 10.0/10.0. Током мастер студија обавила је праксу у Лабораторији за биофизику Института за физику у Београду, где је урадила експериментални део за своју мастер тезу „Одређивање границе просторне резолуције нелинеарне ласерске скенирајуће микроскопије“. 2021. године уписала се на докторске академске студија при Универзитету у Београду, програм Биофизика, и тренутно је на трећој години. Запослена је у Лабораторији за биофизику Института за физику у Београду, у звању истраживач приправник, где се бави истраживањем у области оптичке микроскопије, биофизике и биофотонике. Специјализује се за пројектовање специфичних микроскопских система и њихових потенцијалних примена на узорцима биолошког порекла.

Преглед научне активности

У свом досадашњем раду, Марта Букумира претежно се бавила дизајном, развојем, поставком и применом специјализоване микроскопске технике – нелинеарне ласерске скенирајуће микроскопије (НЛСМ). Предности НЛСМ у односу на друге технике оптичке микроскопије су многоструке, а укључују: снимање узорака у нативном облику, без потребе бојења и припремања узорака; ласерка побуда у инфрацрвеној области, чиме се постиже дубља пенетрација у узорак; знатна редукција ефеката фотоизбељивања; *in vivo* микроскопија, итд. Карактеристике ове технике чине је врло атрактивном за примену на узорцима биолошке природе, што је и примарна сфера интересовања Марте Букумире, као кандидата на докторским академским студијама Биофизика. Нека од истраживања на којима је учествовала: осликавање сигнала трећег хармоника липидних структура у ћелијама гљива и њихова морфолошка анализа, анализа ап-конверторских карактеристика температурно осетљивих наночестица допираних ретким земљама у циљу њихове примене у биомедицини, снимање сигнала другог и трећег хармоника монослојева дихалкогена прелазних метала, итд.

Рад на оваквом систему, Марта Букумира је започела на својим мастер студијама одбранивши мастер тезу „Одређивање границе просторне резолуције нелинеарне ласерске скенирајуће микроскопије“ у оквиру Лабораторије за биофизику Института за физику у Београду, а наставила кроз усавршавање дизајна постојеће експерименталне поставке.

Као чланица тима пројекта *BioPhysFUN*, активно ради на развоју нове интегрисане методе базиране на НЛСМ, која обједињује нелинеарно осликавање, ћелијску хирургију и електрофизиолошку анализу узорака. Поред осликавања, интензивним импулсним ласерима који служе као побуда за НЛСМ, може се вршити и модификација узорака, попут исцртавања произвољних образаца или селективног уклањања дела узорка. Ово је искоришћено као почетна тачка за развој протокола ћелијске хирургије, који ће се усавршавати на поменутој апаратури.

Развој таквог инструмента, као и његова примена на ћелије кончастих гљива, представља фокалну тачку докторске дисертације Марте Букумире, чија је израда одобрена на Већу за интердисциплинарне, мултидисциплинарне и трансдисциплинарне студије, 24. јула 2024. године.

Списак научних радова

Рад у врхунском међународном часопису (**M21**):

1. Jelić JZ, **Bukumira M**, Denčevski A, Senkić A, Žužić L, Radatović B, Vujičić N, Pajić T, Rabasović MD, Krmpot AJ. Application of the Knife-Edge Technique on Transition Metal Dichalcogenide Monolayers for Resolution Assessment of Nonlinear Microscopy Modalities. *Microsc Microanal*. 2024 Aug 21;30(4):671-680. doi: 10.1093/mam/ozae061.

2. Dinić I, Vuković M, Rabanal ME, Milošević M, **Bukumira M**, Tomić N, Tomić M, Mančić L, Ignjatović N. Temperature Sensing Properties of Biocompatible Yb/Er-Doped GdF_3 and YF_3 Mesocrystals. *J. Funct. Biomater*. 2024; 15(1):6. doi: 10.3390/jfb15010006

Саопштења са међународних скупова штампана у целини (**M33**):

1. Vitkovac A, Pajić T, **Bukumira M**, Stanić M, Todorović NV, Rabasović MD. Slight cooling during growth induced changes in filamentous fungi hypha mitochondrial morphology. *2nd International Conference on Chemo and BioInformatics, ICCBIKG*, Kragujevac, Serbia. 2023. doi: 10.46793/ICCBI23.334V

Саопштења са међународних скупова штампана у изводу (**M34**):

1. **Bukumira M**, Vitkovac A, Pajić T, Stanić M, Todorović NV, Rabasović MD. Insights from live non-linear microscopy imaging: comparative analysis of temperature-induced mitochondrial morphology shifts using standard versus machine-learning method. *87th Annual Conference of the DPG and DPG Spring Meeting*, Berlin, Germany. 2024.

2. **Bukumira M**, Jelić J, Denčevski A, Rabasović MD, Vujičić N, Senkić A, Supina A, Krmpot A. Cutting edge technique for determination of spatial resolution limits of nonlinear laser scanning microscopy. *IX International School and Conference on Photonics PHOTONICA2023*. Belgrade, Serbia. 2023.

3. Tomić N, Dinić I, Vuković M, **Bukumira M**, Rabasović MD, Mančić L. One-Step Synthesis of Biocompatible NaY0.65Gd0.15F4:Yb,Er Upconverting Nanoparticles for In

Vitro Cell Imaging. *Serbian Ceramic Society Conference Advanced Ceramics and Application XI New Frontiers in Multifunctional Material Science and Processing,* Belgrade, Serbia. 2023.

4. **Bukumira M**, Jelić J, Denčevski A, Rabasović MD, Vujičić N, Senkić A, Supina A, Krmpot A. Determination of spatial resolution limits of nonlinear laser scanning microscopy. *BPU11 CONGRESS*, Belgrade, Serbia. 2022.

УНИВЕРЗИТЕТ У БЕОГРАДУ

Адреса: Студентски трг 1, 11000 Београд, Република Србија
Тел.: 011 3207400; Факс: 011 2638818; E-mail: kabinet@rect.bg.ac.rs

Београд, 28.08.2024. год
06 Број: 61203-47/ 495-24
JK/

На основу члана 29 Закона о општем управном поступку ("Службени гласник РС", бр. 18/2016 и 95/2018 - аутентично тумачење и 2/2023-одлука УС), а на захтев студенткиње Марта Букумира, издаје се следећа

ПОТВРДА

да је Марта Букумира, рођена 22.03.1996. године у Краљеву, Република Србија, уписана на докторске академске студије: „Биофизика" (180 ЕСПБ) на Универзитету у Београду, у школској 2021/2022. год. Студенткиња је уписала школску 2023/2024. годину у статусу: финансирање из буџета.

Сврха издавања потврде: на лични захтев студента.

Руководилац Службе за студије и науку
Бранка Вукелић

УНИВЕРЗИТЕТ У БЕОГРАДУ

Адреса: Студентски трг 1, 11000 Београд, Република Србија
Тел.: 011 3207400; Факс: 011 2638818; E-mail: kabinet@rect.bg.ac.rs

Београд, 10. јула 2024. године
06 Број: 06-51/III/1639/4-24
ЈКЈ/

На основу члана 50. ст. 4. тач. 3 Статута Универзитета у Београду Статута Универзитета у Београду („Гласник Универзитета у Београду“, број 201/2018, 207/2019, 213/2020, 214/2020, 217/2020, 230/21, 232/22, 233/22, 236/22, 241/22, 243/22, 244/23 и 245/23), а на предлог Већа за студије при Универзитету од 10. јуна 2024. године, Већа за интердисциплинарне, мултидисциплинаре и трансдисциплинарне студије на седници одржаној 10. јула 2024. године, донело је

О Д Л У К У

1. ОДОБРАВА СЕ израда докторске дисертације под насловом: **Развој апаратуре са обједињеним функцијама за осликавање, ћелијску ласерску хирургију и електрофизиолошка мерења на живим ћелијама кончастих гљива**, и испуњености услова кандидата **Букумира Марте** (докторске студије: Биофизика).

2. За менторе се именују:
1. др Александар Крмпот, научни саветник, Институт за физику (физика)
2. др Наташа Тодоровић, виши научни сарадник, Институт за биолошка истраживања „Синиша Станковић“ (биофизика, неурофизиологија)

П Р Е Д С Е Д Н И К
ВЕЋА ЗА ИМТ СТУДИЈЕ

Проф. др Дејан Филиповић

Република Србија
Универзитет у Београду

Оснивач: Република Србија
Дозволу за рад број 612-00-02666/2010-04 од 12. октобра 2011. године је издало Министарство просвете и науке Републике Србије

УБ

Физички факултет, Београд

Оснивач: Република Србија
Дозволу за рад број 612-00-02409/2014-04 од 8. септембра 2014. године је издало Министарство просвете, науке и технолошког развоја Републике Србије

Диплома

Марта, Миодраг, Букумира

рођена 22. марта 1996. године, Краљево, Република Србија, уписана школске 2015/2016. године, а дана 19. септембра 2019. године завршила је основне академске студије, првог степена, на студијском програму Примењена и компјутерска физика, обима 240 (двеста четрдесет) бодова ЕСПБ са просечном оценом 9,72 (девет и 72/100).

На основу тога издаје јој се ова диплома о стеченом високом образовању и стручном називу

дипломирани физичар

Број: 12669000
У Београду, 6. октобра 2021. године

Декан
Проф. др Иван Белча

Ректор
Проф. др Владан Ђокић

00127138

Скенирано помоћу ЦамСканнер-а

Република Србија
Универзитет у Београду

Оснивач: Република Србија
Дозволу за рад број 612-00-02666/2010-04 од 12. октобра 2011. године је издало Министарство просвете и науке Републике Србије

УБ

Физички факултет, Београд

Оснивач: Република Србија
Дозволу за рад број 612-00-02409/2014-04 од 8. септембра 2014. године је издало Министарство просвете, науке и технолошког развоја Републике Србије

Диплома

Марта, Миодраг, Букумира

рођена 22. марта 1996. године, Краљево, Република Србија, уписана школске 2019/2020. године, а дана 27. септембра 2021. године завршила је мастер академске студије, другог степена, на студијском програму Теоријска и експериментална физика, обима 60 (шездесет) бодова ЕСПБ са просечном оценом 10,00 (десет и 0/100).

На основу тога издаје јој се ова диплома о стеченом високом образовању и академском називу

мастер физичар

Број: 12838000
У Београду, 1. новембра 2021. године

Декан
Проф. др Иван Белча

Ректор
Проф. др Владан Ђокић

00128599

Скенирано помоћу ЦамСканнер-а

Application of the Knife-Edge Technique on Transition Metal Dichalcogenide Monolayers for Resolution Assessment of Nonlinear Microscopy Modalities

Jovana Z Jeli, Marta Bukumira, Aleksa Denevski, Ana Senki, Livio Žuži, Borna Radatovi, Nataša Vujii, Tanja Paji, Mihailo D Rabasovi, Aleksandar J Krmpot

DECTRIS

ARINA with NOVENA

Fast 4D STEM

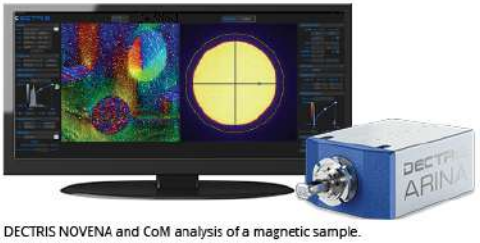

DECTRIS NOVENA and CoM analysis of a magnetic sample.

Sample courtesy: Dr. Christian Liebscher, Max-Planck-Institut für Eisenforschung GmbH.
Experiment courtesy: Dr. Mingjian Wu and Dr. Philipp Pelz, Friedrich-Alexander-Universität, Erlangen-Nürnberg.

Downloaded from https://academic.oup.com/mam/advance-article/doi/10.1093/mam/ozae061/7712562 by Dusan Spasojevic user on 12 July 2024

Microscopy and Microanalysis, 2024, **00**, 1–10
https://doi.org/10.1093/mam/ozae061

Original Article

Microscopy AND Microanalysis

Application of the Knife-Edge Technique on Transition Metal Dichalcogenide Monolayers for Resolution Assessment of Nonlinear Microscopy Modalities

Jovana Z. Jelić[1], Marta Bukumira[1], Aleksa Denčevski[1], Ana Senkić[2], Livio Žužić[3], Borna Radatović[4], Nataša Vujičić[2], Tanja Pajić[5], Mihailo D. Rabasović[1], and Aleksandar J. Krmpot[1,*]

[1]*Institute of Physics Belgrade, University of Belgrade, National Institute of the Republic of Serbia, Pregrevica 118, Belgrade 11080, Serbia*
[2]*Centre for Advanced Laser Techniques, Institute of Physics Zagreb, Bijenička cesta 46, Zagreb 10000, Croatia*
[3]*Department of Physics, University of Zagreb, Bijenička cesta 32, Zagreb 10000, Croatia*
[4]*Materials Science Factory, Instituto de Ciencia de Materiales de Madrid (ICMM-CSIC), Sor Juana Ines de la Cruz 3, Madrid 28049, Spain*
[5]*Department for General Physiology and Biophysics, Faculty of Biology, University of Belgrade, Studentski trg 16, Belgrade, 11158, Serbia*

***Corresponding author:** Aleksandar J. Krmpot, E-mail: krmpot@ipb.ac.rs

Abstract

We report application of the knife-edge technique at the sharp edges of WS_2 and MoS_2 monolayer flakes for lateral and axial resolution assessment in all three modalities of nonlinear laser scanning microscopy: two-photon excited fluorescence (TPEF), second- and third-harmonic generation (SHG, THG) imaging. This technique provides a high signal-to-noise ratio, no photobleaching effect and shows good agreement with standard resolution measurement techniques. Furthermore, we assessed both the lateral resolution in TPEF imaging modality and the axial resolution in SHG and THG imaging modality directly via the full-width at half maximum parameter of the corresponding Gaussian distribution. We comprehensively analyzed the factors influencing the resolution, such as the numerical aperture, the excitation wavelength and the refractive index of the embedding medium for the different imaging modalities. Glycerin was identified as the optimal embedding medium for achieving resolutions closest to the theoretical limit. The proposed use of WS_2 and MoS_2 monolayer flakes emerged as promising tools for characterization of nonlinear imaging systems.

Key words: knife-edge technique, nonlinear laser scanning microscopy, resolution measurement, second/third harmonic generation, WS_2 and MoS_2 monolayers

Introduction

Nonlinear laser scanning microscopy (NLSM) is a specialized microscopy technique that uses localized nonlinear excitation to excite fluorescence only within a thin raster-scanned plane. In NLSM, two-photon excited fluorescence (TPEF) is typically detected and used for imaging (Masters & So, 2009; Tserevelakis et al., 2012; Rohrbacher et al., 2017). In addition to TPEF, other imaging techniques include three-photon excited fluorescence, and second- and third-harmonic generation (SHG, THG) (Zipfel et al., 2003; Tserevelakis et al., 2010).

Every optical system has a fundamental limitation of resolution due to diffraction which causes the image to spread in both lateral and axial directions. The diffraction pattern (light intensity distribution) of a point-like light source in the lateral (x,y) and axial (z) dimensions is referred to as a point-spread function (PSF) (Cole et al., 2011). According to the Houston criterion for resolution (van den Bos & den Dekker, 2001), two point sources are considered resolved if the full-width at half maximum (FWHM) of their PSFs no longer overlap. In microscopy, resolution depends on many factors such as numerical aperture (NA) of the objective lens, wavelength, refractive index of the embedding medium, coverglass thickness, distance between the object and coverglass, etc. (Kozubek, 2001).

The standard technique for evaluating resolution is based on the imaging of nanospheres, often referred to as beads. Beads can be used directly to assess lateral resolution, or to determine the PSF by applying the deconvolution method (using bead images and prior knowledge of the actual bead size). Although this method is practical, it does have certain limitations. As bead size decreases, the signal-to-noise ratio (SNR) deteriorates, making it challenging to obtain reliable measurements. Deconvolution, on the other hand, can be severely affected by noise. With axial resolution, the stack image of the beads must be recorded. This is challenging in practice as the beads are prone to photobleaching. Consequently, the measurement of axial resolution results in a relatively small number of data points which affects the quality of the assessment. Furthermore, due to the coherent nature of the SHG signal, its PSF is a contentious issue, as pointed out in Chen et al. (2012). Accordingly, imaging of common polystyrene beads by SHG microscopy is not widely used and has been reported only in terms of the material nonlinear response characterization, with no resolution assessment (Hou & Labarthet, 2018). Similarly, sparse THG imaging of similar objects for resolution measurement was demonstrated in Masihzadeh et al. (2009). Several inorganic nanocrystals of noble metals or metal oxides arranged in a noncentrosymmetric crystal structure

Received: February 5, 2024. **Revised:** June 19, 2024. **Accepted:** June 23, 2024
© The Author(s) 2024. Published by Oxford University Press on behalf of the Microscopy Society of America. All rights reserved. For commercial re-use, please contact reprints@oup.com for reprints and translation rights for reprints. All other permissions can be obtained through our RightsLink service via the Permissions link on the article page on our site—for further information please contact journals.permissions@oup.com.

Downloaded from https://academic.oup.com/mam/advance-article/doi/10.1093/mam/ozae061/7712562 by Dusan Spasojevic user on 12 July 2024

(such as $KTiOPO_4$) have been used as point-like SHG signal sources in NLSM (Mahou et al., 2017), in a manner similar to beads. In contrast to fluorescence, SHG is theoretically an achromatic phenomenon which can be obtained at arbitrary wavelengths covering the entire range of tunable NIR lasers. This makes such crystal structures suitable for NLSM resolution evaluation.

Due to the lack of techniques for assessing resolution of all three modalities of NLSM (TPEF, SHG, and THG) within a single microscopic system, we were inspired to conduct a more in-depth investigation into this matter. Here, we propose application of the knife-edge technique to monolayers of transition metal dichalcogenides (TMDs), in particular WS_2 and MoS_2, for evaluation of lateral resolution. In their single-layer form, TMDs have a D_{3h} symmetry where the lack of inversion symmetry allows for an unusually strong SHG signal. This effect is very sensitive to layer thickness, crystalline orientation, and layer stacking (Kumar et al., 2013; Yin et al., 2014; Rosa et al., 2018). The thickness of our samples (<1 nm) (Radisavljevic et al., 2011) and their efficient SHG production (Woodward et al., 2016) and THG (Wang et al., 2013) signals also allow direct measurement of axial resolution. The intensity profiles obtained at the monolayer-substrate boundary are free from artifacts typically associated with thicker samples. Although a similar approach was reported by Mehravar et al. (2020), the absence of axial resolution results in their study can be attributed to excessive thickness of the samples used. Other 2D materials (2DMs) such as hBN have been reported as a test material in resolution assessment of a confocal focus-engineered coherent anti-Stokes Raman scattering (cFE-CARS) microscope (Lee et al., 2023). However, h-BN exhibits an SHG signal that is an order of magnitude lower than that of the MoS_2 monolayer (Li et al., 2013). SHG and THG signals obtained by WS_2 and MoS_2 monolayers both result in a relatively high SNR and no photobleaching effect.

While the knife-edge technique is commonly used for laser beam profile determination (Araújo et al., 2009), its application in resolution assessment of various microscopic techniques (Chu et al., 2005; Wachulak et al., 2017; Mennel et al., 2018; Mylonakis et al., 2024) has generally been limited and auxiliary. The knife-edge technique is a method of assessing resolution by analyzing the transition zone across a boundary formed by sharp-edged objects. By extracting intensity profiles across the edge and measuring the width and slope, one can determine the resolution of an optical system. A sharper and narrower transition generally indicates a higher resolution, while a wider transition indicates a lower resolution. In this study, we present the measurement of resolution in different imaging modalities of our custom-built nonlinear laser scanning microscope (Rabasovic et al., 2015) utilizing two distinct approaches.

Here, we report application of the knife-edge technique on WS_2 and MoS_2 (for lateral resolution assessment in SHG and THG modalities). We also evaluated both lateral (in TPEF modality) and axial resolution (in SHG and THG modalities) directly via the FWHM parameter of the corresponding Gaussian distribution. Our study includes a comprehensive analysis of how the resolution varies with the NA of the objective lens, excitation wavelengths, refractive index of the embedding medium, and imaging modality of the microscope. In addition, the obtained PSF (FWHM) values were employed in deconvolution of the image, resulting in significant improvement in image resolution.

Materials and Methods

NLSM Experimental Setup

Our custom-made NLSM system [detailed information can be found in Pajić et al. 2022] enables precise control of power levels and motorized positioning of the sample in the axial direction with a minimum step-size of 0.25 μm. For TPEF and SHG imaging, a tunable (700–1,000 nm) Kerr lens mode-locked femtosecond Ti: Sapphire laser (Mira 900, Coherent Inc., CA, USA) with a repetition rate of 76 MHz and pulse duration of 160 fs was used. Femtosecond pulses were also obtained from a SESAM mode-locked Yb:KGW laser (Time-Bandwidth Products AG, Time-Bandwidth Yb GLX; Zurich, Switzerland) at a fixed wavelength of 1,040 nm with a pulse duration of 200 fs and a repetition rate of 83 MHz. After being expanded 3.75 times with a Keplerian telescope (obtained by AC254-040-A and AC254- 150-A lenses, both from Thorlabs, Inc.), the laser beams are directed toward the objective lens via a main dichroic mirror (MDM; FF700-SDi01-25x36, Semrock). Beam raster scanning over the sample is achieved using a galvo scanner (6,215H, Cambridge Technologies). A National Instruments USB-6351 card was used for signal acquisition and control of the galvo scanner with a sampling rate of 1.2 M sample/s.

SHG and TPEF signals were collected in back reflection by an objective lens, passed through the MDM, filtered with appropriate filters (depending on the excitation wavelengths used and imaging modality), and then focused onto a photomultiplier tube (PMT) (RCA, PF10006). In SHG modality, we used several narrow bandpass filters (FBH370-10, FBH400-10, FBH420-10, and FB520-10, all from Thorlabs, Inc.). In the TPEF modality, the signal was filtered with a shortpass filter (FESH0700, Tholarbs, Inc.). In THG imaging, the signal was detected in the forward direction (transmission arm) after being reflected by two harmonic beam splitters (HBSY13, Thorlabs, Inc.) to reduce reflection of laser light. Finally, the residual laser light was filtered out by two filters (FGUV11M, Thorlabs, Inc. and FSR-U340, Newport). After filtering, the THG signal was focused onto the entrance window of the PMT (H7422, Hamamatsu, Japan).

Fluorescent Beads

To measure lateral resolution in TPEF modality, we used a TetraSpeck Fluorescent Microspheres Size Kit (Invitrogen, Thermo Fisher Scientific Inc.) which was specially developed for the calibration of microscopes. The slide contains six viewing areas, each of which contains nanospheres of a specific (nominal) size: 0.1 μm, 0.2 μm, 0.5 μm, 1.0 μm, or 4.0 μm and a mixture of all sizes. Each nanosphere is stained with four different fluorescent dyes: 365/430 nm, 505/515 nm, 560/580 nm, and 660/680 nm. This makes them suitable for applications that require a broad spectral range. For the purpose of resolution measurements, the optimal SNR was obtained for 0.2 μm fluorescent beads. The profile extracted from the recorded images of the beads was fitted by the Gaussian function. The lateral resolution was directly assessed through the FWHM parameter of the Gaussian fit.

WS_2 and MoS_2 Monolayers

Synthesis

MoS_2 samples were synthesized using a chemical vapor deposition (CVD) technique, described in detail in Senkić et al. (2023). Samples were grown on two substrates: c-cut sapphire

Downloaded from https://academic.oup.com/mam/advance-article/doi/10.1093/mam/ozae061/7712562 by Dusan Spasojevic user on 12 July 2024

and Si/SiO_2, each with a 290 nm oxide layer thickness. The synthesis procedure is the same as described in Senkić et al. (2023), with a growth temperature, T_G, equal to 875 C. The thickness of monolayers was determined using atomic force microscopy (AFM), and was determined to be 0.8 nm Senkić et al. (2023).

Similar to the MoS_2 growth, DI water-based solutions were used for WS_2. As a growth promotor, a 5 ppm concentration of NaOH solution was used, whereas the tungsten source was a 100 ppm concentration of ammonium metatungstate hydrate $(NH_4)_6H_2W_{12}O_{40}$ H_2O (99.99% Sigma Aldrich). These solutions were mixed in equal parts, and the 10 μL droplet of this mixture was dropcast onto the cleaned substrate, which were then placed on a hot plate at 120 C until the droplet dried. The Si/SiO_2 substrate was first cleaned with argon gas, and then in an O_2 plasma chamber for 10 min. Before loading the substrate with the deposited metal precursor, the CVD furnace was heated to 500 C under argon flow ($\zeta = 200$ sccm). When the substrate was loaded, the furnace temperature was raised to the growth temperature of 850 C. The sulfur temperature was set to 140 C, and argon flow to 100 sccm. When both temperatures reached their target value, the argon flow was decreased to 75 sccm and the synthesis process was started. After 5 min, the furnace was then quickly cooled to 775 C using compressed air with the argon flow set to 50 sccm, whereas the sample remained in the furnace. Then, the argon flow was stopped ($\zeta = 0$ sccm), the furnace further cooled to 500 C, and the sample was completely removed from the CVD furnace.

Transfer

MoS_2 and WS_2 were moved from the Si wafer by using polydimethylsiloxane (PDMS) transfer (Niehues et al., 2018). The first step is a pickup, in which 2DMs are moved from the growth substrate on the PDMS sheet. In this step, the PDMS sheet (160 μm thick) purchased from GEL-PAK company was cut into a rectangle slightly larger than the Si/SiO_2 substrate and positioned on top of the Si/SiO_2 surface with 2DMs. To increase the separation speed in the following phase, PDMS is left without contact on one of the edges of the Si/SiO_2 substrate, which was ensured by placing a carbon fiber or any similar object on the substrate edge before placing PDMS on top. Subsequently, the PDMS/2DM/substrate is placed on top of a DI (deionized) water and ammonia solution (1,000:1 ratio), which is gently stirred to ensure the flow of the solution. The solution slowly intercalates between the PDMS and Si/SiO_2 substrate, separating 2DM from the Si/SiO_2 substrate. After complete separation in a few minutes, the Si/SiO_2 substrate sinks into the solution, and PDMS with 2DM are left floating on top of the solution. PDMS with 2DM is additionally rinsed with DI water and dried with nitrogen flow to remove residual water from the surface.

For placing 2DMs from PDMS on sapphire, PDMS with 2DM is positioned on top of the sapphire and gently pressed with an Q-tip to ensure adequate adhesion over the whole surface. PDMS with 2DM is fixed on a z-axis manipulator with which the separation of PDMS and sapphire can be controlled. To ensure that the 2DM has higher adhesion with sapphire, PDMS is slowly separated in small steps with a z-axis manipulator. The front of the adhesion is monitored with an optical microscope to increase separation speed in areas of no interest and reduce it in regions with 2DM flakes. After the controlled and complete separation of PMDS, 2DM is left on the sapphire surface. For detailed information about this process, see Castellanos-Gomez et al. (2013).

Sample Preparation

The MoS2 and WS2 substrate monolayers were placed on a microscopic slide and fixed with a coverslip, leaving the layer of air between the two glass surfaces. In addition, we introduced various media with different refractive indices to the monolayers. A small amount of glycerin, with a refractive index of $n = 1.47$ was directly applied on top of the monolayers and then fixed with a coverslip. Distilled water was also used as an embedding medium, but without a coverslip as we employed a "water-dipping" objective lens for this type of samples. During the recording in different embedding media, no degradation of monolayer flakes was observed, so samples prepared in this way can be used several times. This approach allowed us to systematically examine how different embedding media influence resolution assessment.

Objective Lenses

We used a range of objective lenses (see Table 1) to investigate how resolution assessment is affected by different measurement conditions. A variety of different objective lenses was used, taking into account their different NA's, magnifications and using different immersion media. For samples embedded in distilled water, we employed the water-dipping objective lens, specifically W Plan-APOCHROMAT. This type of objective lens is designed to be used without a coverslip, with the tip submerged into the embedding medium.

Theoretical Limit Calculation

The theoretical limits for the lateral and axial resolutions under the different measurement conditions given in this paper were calculated using the following equations (Squier &

Table 1. Overview of Objective Lenses Used (All from Zeiss)

Objective lens	Magnification	Numerical aperture	Immersion	Working distance (mm)	Chromatic aberration correction	Spherical aberration correction
EC Plan-NEOFLUAR	40×	1.30	Oil	0.21	Red and blue; green close	Blue, green
W Plan-APOCHROMAT	40×	1.00	Water-dipping	2.50	Deep blue, blue, green and red	Deep blue and blue
Plan-APOCHROMAT	20×	0.80	—	0.55	Deep blue, blue, green and red	Deep blue and blue
GF Planachromat	40×	0.65	—	0.53	Red and blue	Green

Downloaded from https://academic.oup.com/mam/advance-article/doi/10.1093/mam/ozae061/7712562 by Dusan Spasojevic user on 12 July 2024

Müller, 2001; van den Bos & den Dekker, 2001; Masters & So, 2009; Farahi, 2015):

$$\mathrm{FWHM}_{\mathrm{lat}} = \frac{1}{N}\frac{0.51\ \lambda}{\mathrm{NA}} \quad (1)$$

$$\mathrm{FWHM}_{\mathrm{ax}} = \frac{1}{N}\frac{1.77\ n\ \lambda}{\mathrm{NA}^2} \quad (2)$$

with λ representing excitation wavelength, n is the index of refraction of respective embedding media, and N is the nonlinearity order ($N = 2$ for TPEF and SHG, $N = 3$ for THG). We should emphasize that the magnitude for NAs used in all calculation throughout the paper were from the specifications of the objective lenses given by the manufacturer. This can be considered as the best possible approximation as the exact magnitude is only valid under certain conditions (refractive index of the sample/embedding medium and proximity to the coverslip surface) and may vary with different settings/conditions. In other words, if the embedding medium is changed, the refractive index changes and so does the NA which depends on the refractive index. This change cannot be measured or estimated, so the value from the objective specification is used in the calculations for all settings/conditions.

Results

Lateral Resolution in TPEF Modality

WS_2 and MoS_2 monolayers can generate photoluminescence when excited in the 520–640 nm and 610–670 nm ranges (Rigosi et al., 2015). Therefore, they can be used for resolution assessment of fluorescence microscopy modalities in general. However, due to the spectral range of our lasers, it was not possible to obtain a TPEF signal from these monolayers. Therefore, we opted to use 0.2 μm fluorescent spheres to access lateral resolution. The inset in Figure 1 shows the fluorescent spheres recorded in the TPEF modality using the 40 × 1.3 objective lens. By fitting the extracted intensity profile using a Gaussian function, we determined the lateral resolution to be (320 ± 20) nm. The data points for fitting were chosen to include the feature of interest (i.e., peak), while expanding the range did not affect the fitting parameters. The result corresponds to the FWHM of the obtained intensity distribution, with the error representing the fitting error. The lateral resolution in the TPEF modality was only successfully determined at an excitation wavelength of 730 nm. The theoretical limit for lateral resolution in the TPEF modality, which was calculated under the same conditions according to the equation (1), is 203 nm. Excitation at higher wavelengths resulted in insufficient SNR for the resolution measurement. It was not possible to record a stacked image of satisfactory quality for axial resolution assessment due to pronounced photobleaching. It is also important to note that the fluorescent spheres used in this case cannot be considered as point-like sources due to their size and expected resolution. In contrast, the use of TMD monolayers does not lead to photobleaching and eliminates the need for deconvolution due to their subnanometer thickness. Consequently, the application of knife-edge technique to TMD monolayers provides a reliable measurement of both lateral and axial resolution.

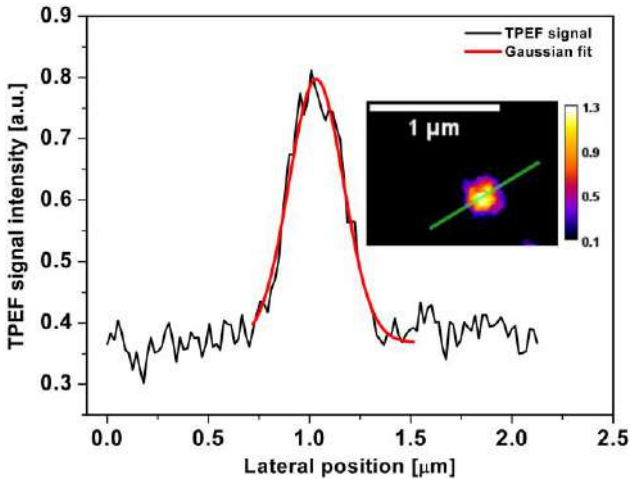

Fig. 1. TPEF signal of a fluorescent bead with a nominal size of 0.2 μm. The individual intensity profile was extracted from the labeled position on the inset. The profile was fitted using a Gaussian function with a quality indicator for the fit of $R^2 = 97.5$. The sample was recorded using a 40 × 1.3 objective lens at the excitation wavelength of 730 nm.

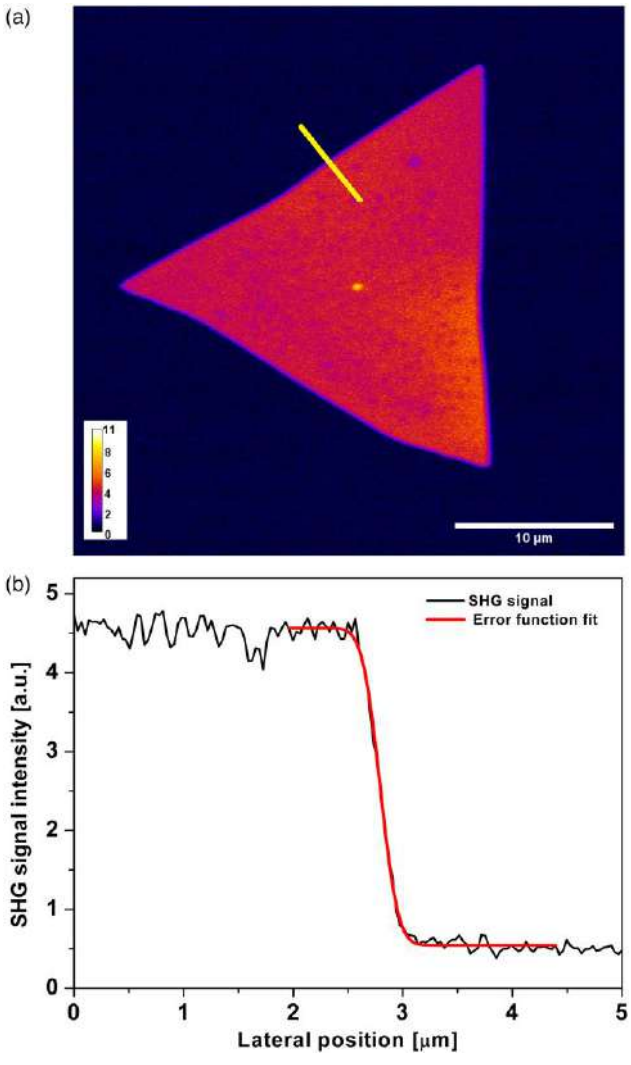

Fig. 2. (**a**) SHG image of a MoS_2 flake. The image was recorded at an excitation wavelength of 800 nm using a 40 × 1.3 objective lens with glycerin as the embedding medium. The marker (line) indicates the position along the edge of the monolayer flake from which the intensity profile was extracted. (**b**) Typical intensity profile extracted at the edge of the MoS_2 monolayer flake. The profile was fitted using the error function, with the parameter for the quality of fit $R^2 = 99.8$.

Downloaded from https://academic.oup.com/mam/advance-article/doi/10.1093/mam/ozae061/7712562 by Dusan Spasojevic user on 12 July 2024

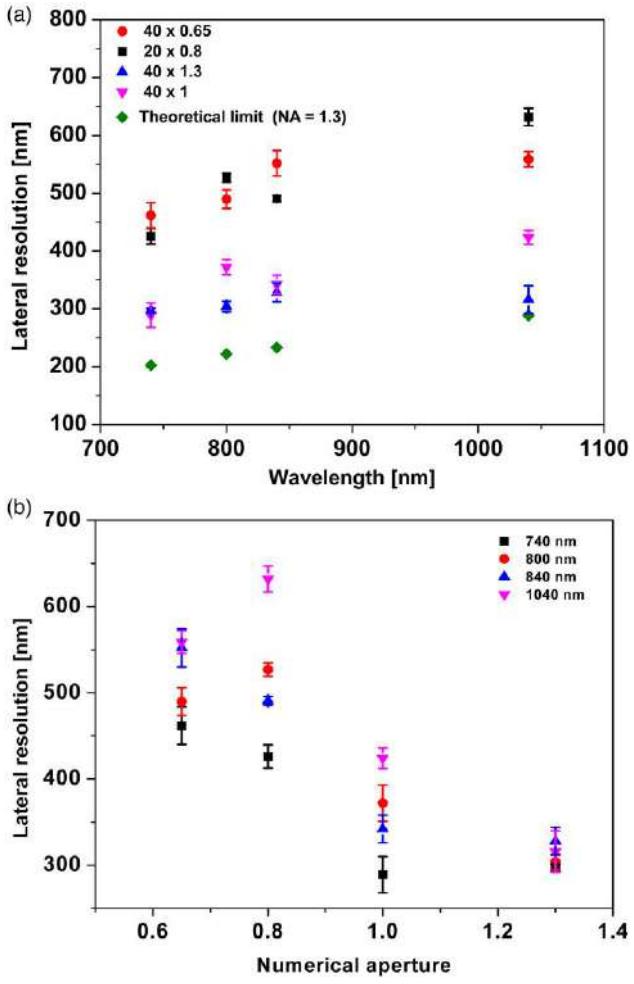

Fig. 3. Dependence of the lateral resolution on (**a**) the excitation wavelength for various objective lenses and (**b**) the numerical aperture for various excitation wavelengths. The results were obtained for a MoS_2 monolayer in the SHG modality.

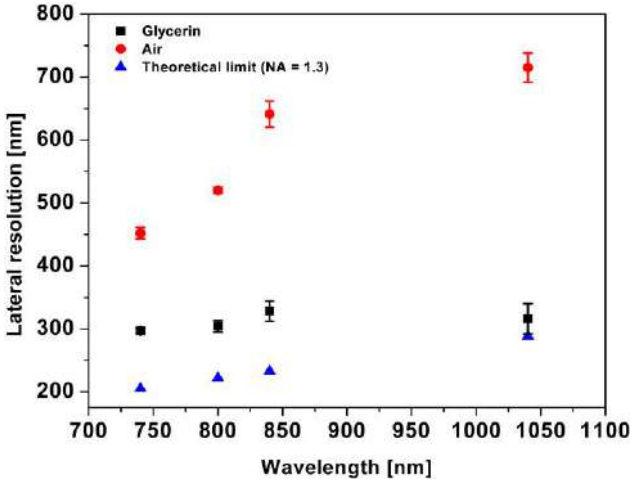

Fig. 4. Dependence of the lateral resolution on the excitation wave length for two embedding media, air, and glycerin. The graph shows the results obtained with a 40 × 1.3 objective lens and the theoretical limit for the lateral resolution under the same measurement conditions. The results were obtained for a MoS_2 monolayer in the SHG modality.

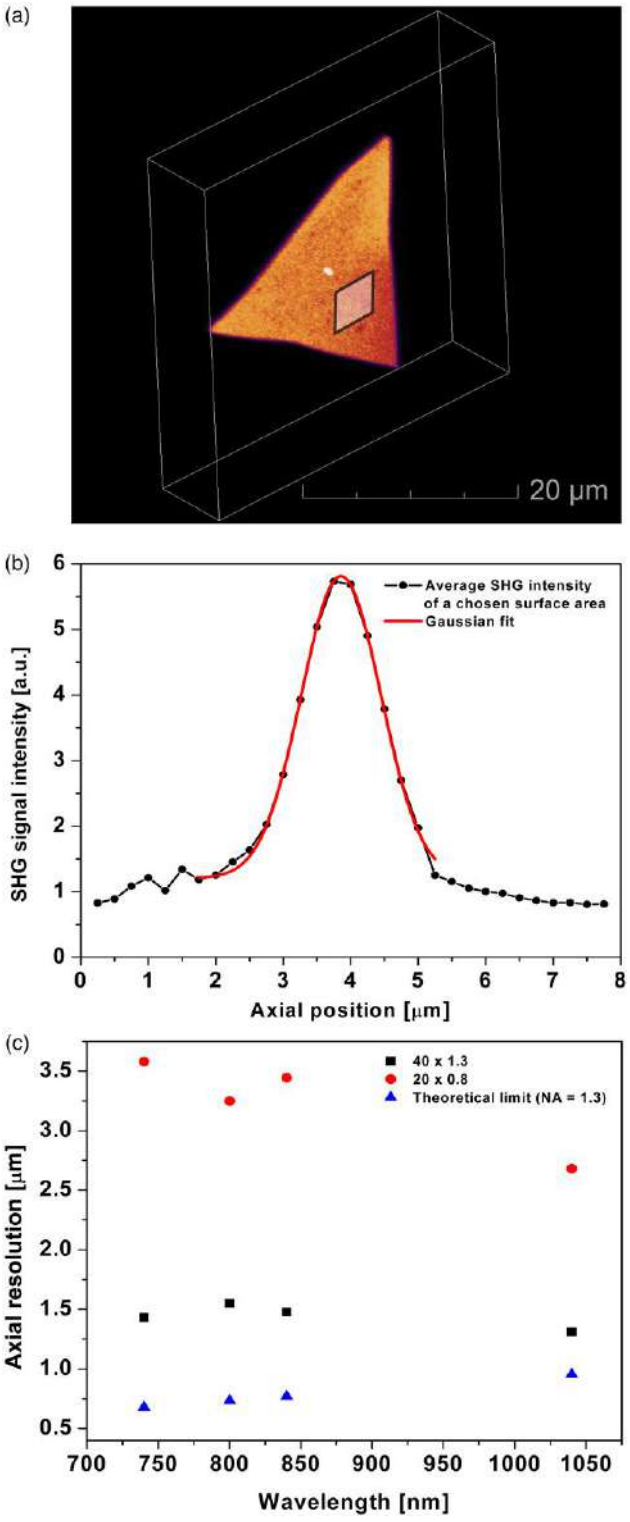

Fig. 5. (**a**) Calibrated 3D model of the MoS_2 monolayer flake with labeled surface from which the average intensity was calculated. (**b**) Intensity profile obtained by averaging the intensity of a chosen surface area of 100 × 100 pixels for each image of the flake in the stack. The *x*-axis represents the axial position of the image plane. The fitting was performed using Gaussian fit, with the quality parameter $R^2 = 99.7$. (**c**) Dependence of the axial resolution on the excitation wavelengths in the SHG modality for 40 × 1.3 and 20 × 0.8 objective lenses.

Downloaded from https://academic.oup.com/mam/advance-article/doi/10.1093/mam/ozae061/7712562 by Dusan Spasojevic user on 12 July 2024

Resolution Assessment in SHG Modality

MoS_2 and WS_2 monolayers were used for resolution measurement in the SHG modality. No significant differences in the resolution assessment were found between these two materials. The typical image of a monolayer flake is shown in Figure 2a. These flakes exhibit distinct and well-defined edges, suitable for lateral resolution assessment using the knife-edge technique. To determine lateral resolution, we extracted intensity profiles over the edge and performed fits using the error function (which is the integral of the Gaussian function) (Davis & Brown, 2002), as shown in Figure 2b. The data points for the fit were chosen to include features of interest (the slope), while further expansion of the range did not affect the fit parameters. The intensity profiles of the monolayer-substrate boundary were analyzed at typically ten different positions along the edge, resulting in a total of 800 processed profiles. The lateral resolution was then calculated based on the mean value of the parameter w (the half-width at $\frac{1}{e^2}$ of the corresponding Gaussian distribution) obtained for each processed monolayer flake, with the error corresponding to the standard error of the mean. The resolution is presented as FWHM of the Gaussian distribution corresponding to the data obtained, where FWHM is calculated as $w/0.85$.

The axial resolution was determined based on the recorded stack, a series of consecutive images taken in equidistant sample planes, of a thin monolayer. A homogeneous surface of approximately 100 × 100 pixels was selected within the monolayer. The same surface was analyzed on all images of the stack. The average value of the pixel intensity of the observed surface was determined. The dependence of the average intensity of the chosen surface area on the corresponding axial position of the image plane was fitted by the Gaussian function. The FWHM parameter of the Gaussian fit was read directly as the axial resolution of the microscope under the specified conditions, with the error corresponding to the fitting error.

Both lateral and axial resolutions were presented as the FWHM values, all in accordance with the Houston criterion for resolution. An identical data analysis procedure was applied for resolution assessment in THG modality.

Table 2. Comparison of Axial Resolutions in SHG Modality between Different Embedding Media and Objective Lenses, along with the Theoretical Limits Provided in Brackets.

SHG	740 nm	800 nm
Glycerin	1.4 μm (0.81 μm)	1.6 μm (0.87 μm)
Air	5.9 μm (0.55 μm)	6.7 μm (0.59 μm)

The theoretical limits were calculated using the equations (1) and (2) with the refractive indices of glycerin and air: $n = 1.47$ and $n = 1$, respectively.

Lateral Resolution in SHG Modality

To investigate wavelength-dependent variation in lateral resolution of the microscope, we recorded SHG signal of the monolayer flake at four different excitation wavelengths: 740 nm, 800 nm, 840 nm, and 1,040 nm, using glycerin as the embedding medium. The dependence of the resolution on wavelength for different NA's of objective lenses is shown in Figure 3a. The graph illustrates the theoretical limit of lateral resolution for the objective lens with a numerical aperture of 1.3 at different wavelengths. The experimental results align with expectations and show a deterioration of resolution with increasing wavelength for the specific objective lens. A lower value indicates better resolution and vice versa. An exception was noted at 800 nm, where better resolution was achieved with a lower NA objective lens (0.8 versus 0.65). A similar apparent exception was also observed at 740 nm (1.0 versus 1.3), which is within the experimental margin of error. Additionally, the obtained values are above the theoretical limit at all wavelengths. Figure 3b shows the dependence of the lateral resolution on the NA of the corresponding objective lenses for different wavelengths. The results are generally in line with expectations, with two exceptions observed for objective lenses with NA values of 0.8 and 1.0, where better resolution was achieved at 840 nm compared to 800 nm. The aforementioned exceptions might be attributed to the fact that the objective lenses used in this study are not designed for infrared light but for visible light (see Table 1), resulting in suboptimal focusing. This may vary from case to case (for different objectives, at different wavelengths). The lateral resolution for the 40 × 1.3 objective lens exhibits weak wavelength dependence, which agrees well with the theoretical limit shown in Figure 3a. As the monolayer flakes are significantly thinner than the expected resolution, deconvolution is not required. Notably, no photobleaching of the samples was observed at any wavelength during monolayer imaging.

In addition to the factors already mentioned, resolution is further influenced by the order of interaction. While TPEF

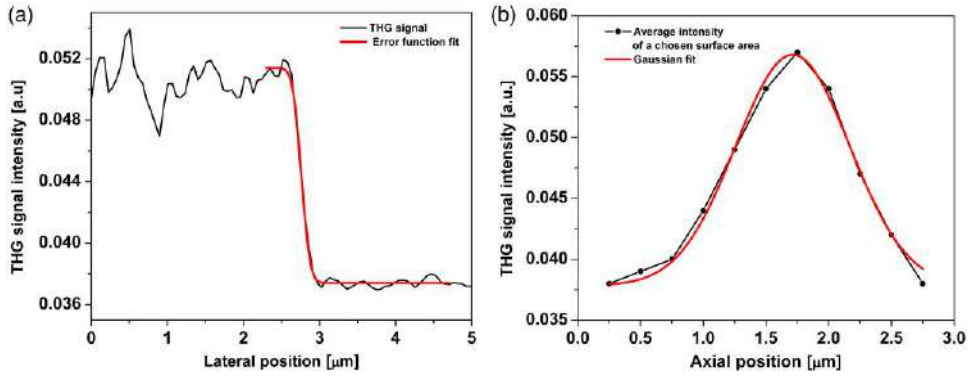

Fig. 6. (**a**) Typical intensity profile extracted at the edge of the WS_2 monolayer flake in THG modality for a 40 × 1.3 objective lens. The profile was fitted using the error function, with the quality of fit parameter $R^2 = 99.6$. (**b**) Intensity distribution obtained by averaging the intensity of a chosen area of 60 × 60 pixels for each image in the stack. The *x*-axis represents the axial position of the image plane. Fitting was performed using the Gaussian function, with the quality parameter of fit $R^2 = 99$.

Downloaded from https://academic.oup.com/mam/advance-article/doi/10.1093/mam/ozae061/7712562 by Dusan Spasojevic user on 12 July 2024

and SHG are conceptually distinct processes, both involve two-photon interactions, suggesting that the resolutions obtained for the corresponding imaging modalities should be closely aligned. This implies that the theoretical limit will be the same for both imaging modalities at a given wavelength. Despite the slightly higher excitation wavelength of 740 nm used for the resolution measurement in the SHG modality, the measured resolution of (300±10) nm exceeds that of the TPEF modality (320±20) nm obtained at 730 nm. However, this statement is not conclusive as the measurements are within the margin of error. Both measurements were performed using a 40 × 1.3 objective lens. The fluorescent beads utilized in our study do not serve as ideal point-like sources for resolution measurement. In contrast, monolayer flakes due to their extensive thinness, offer a better approximation when combined with the knife-edge technique.

Using the same method, we also investigated the influence of the embedding medium on the lateral resolution of the SHG modality. We recorded images of monolayer flakes at various excitation wavelengths using a 40 × 1.3 objective lens, with one sample embedded in glycerin and the other in air. Figure 4 illustrates the lateral resolution for the two specified embedding media. It is shown that the resolution is closer to the theoretical limit when glycerin is present at all excitation wavelengths used, indicating a more appropriate utilization of the objective lens.

Axial Resolution in SHG Modality

In addition to assessing lateral resolution, we also investigated axial resolution using the same samples. The SHG signal of glycerin-embedded monolayer flakes was recorded at various excitation wavelengths. For each wavelength, a stack of typically 30 images was acquired, with a slice spacing of 0.25 μm. To determine the axial resolution at a specific wavelength, we selected a homogeneous surface area from each image of the stack. Figure 5a displays the calibrated 3D model of the monolayer flake and provides an example of the surface used to derive parameters for axial resolution assessment. The resolution was determined based on the dependence of average intensity of the chosen surface area on the corresponding axial position of the image plane in the stack. This is shown in Figure 5b. This dependence was fitted with a Gaussian function and the FWHM was determined as a measure of resolution. The measurement involved two objective lenses with distinct NA values with an aim to investigate how the resolution varies with the NA for different wavelengths. The corresponding results are shown in Figure 5c together with the theoretical resolution limit in the case of an objective lens with an NA value of 1.3. Although the obtained resolution is above the theoretical limit, the observed trend deviates from expectations and indicates an improvement in resolution with increasing wavelength, which is particularly evident for the 20 × 0.8 objective lens. A similar trend can be seen for the 40 × 1.3 objective lens. As expected, superior results were consistently obtained with the higher NA objective lens.

We also investigated how axial resolution is affected by the embedding medium. The SHG signal of MoS_2 monolayer flakes was recorded using a 40 × 1.3 objective lens at excitation wavelengths of 740 nm and 800 nm, using glycerin and air as embedding media. A comparison between the axial resolutions obtained for different embedding media is provided in Table 2. Significantly poorer results were obtained when air was used as the embedding medium.

Table 3. Comparison of Lateral and Axial Resolution in THG Modality between Different Embedding Media and Objective Lenses, along with the Theoretical Limits Provided in Brackets.

THG (1,040 nm)	Lateral Resolution (μm)		Axial Resolution (μm)
	20 × 0.8	40 × 1.3	40 × 1.3
Glycerin	0.44 (0.39)	0.27 (0.24)	1.10 (0.92)
Air	0.75 (0.39)	0.43 (0.24)	5.90 (0.63)

The theoretical limits were calculated using the equations (1) and (2) with the refractive indices of glycerin and air: $n = 1.47$ and $n = 1$, respectively.

Resolution Assessment in THG Modality

We measured both lateral and axial resolution of the microscope in the THG modality using WS_2 monolayer flakes immersed in glycerin with an excitation wavelength of 1,040 nm and a 40 × 1.3 objective lens. Figure 6a shows a typical intensity profile extracted from the edge of the monolayer flake. This profile was fitted with the error function, resulting in a lateral resolution of (270 ± 10) nm. Figure 6b shows the distribution of the average intensities of the selected surface area from each image of the stack (slice separation of 0.25 μm) over the axial position of the image plane. Using this profile, we were able to determine the axial resolution to be (1.07 ± 0.06) μm. We investigated how both the lateral and axial resolution in THG modality vary between different embedding media and objective lenses. An overview of the results is displayed in Table 3, which quantifies the effect of embedding media with different refractive indices on image

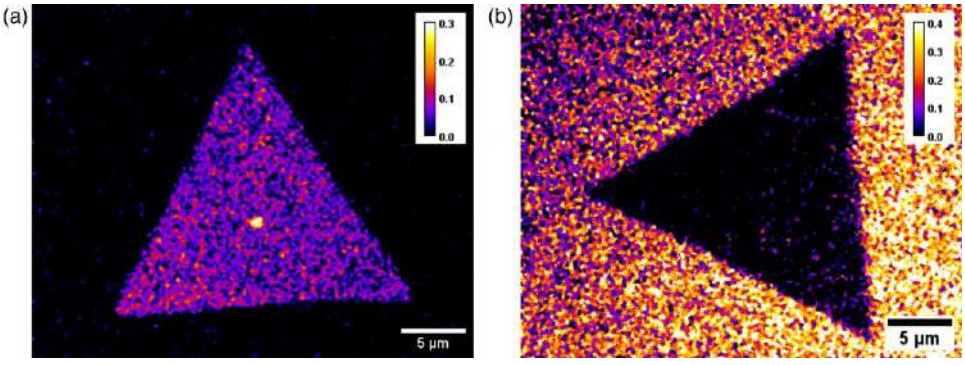

Fig. 7. (**a**) MoS_2 monolayer flake with glycerin as the embedding medium. (**b**) MoS_2 monolayer flake with air as embedding medium. The figure clearly shows decreasing of the THG signal in air.

Downloaded from https://academic.oup.com/mam/advance-article/doi/10.1093/mam/ozae061/7712562 by Dusan Spasojevic user on 12 July 2024

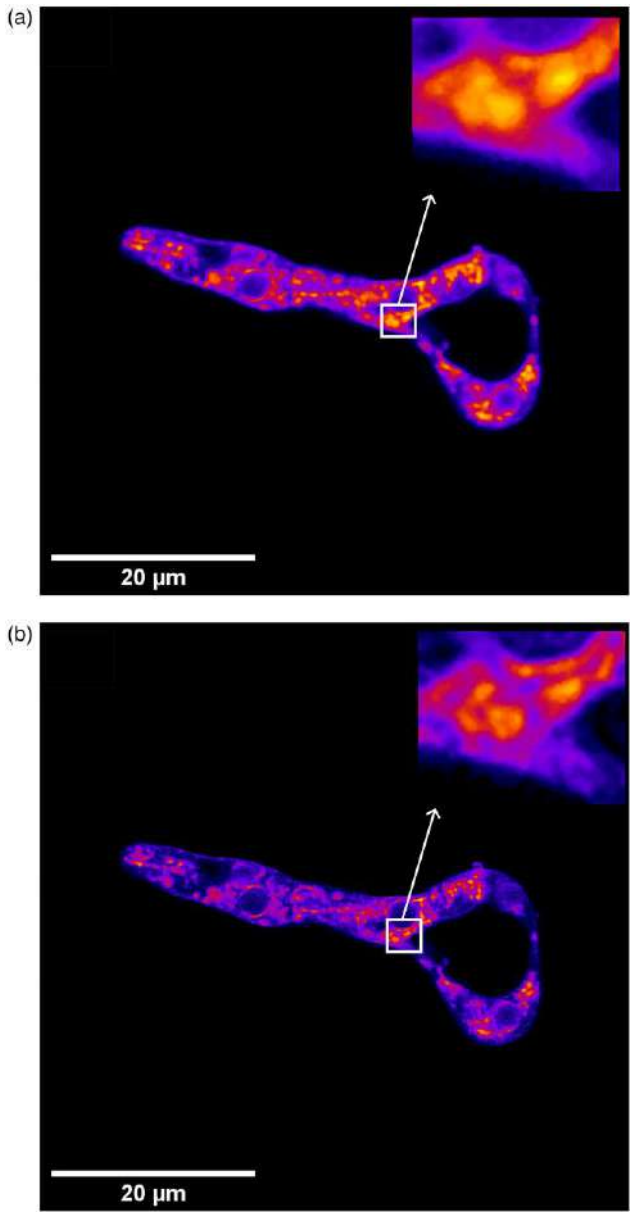

Fig. 8. TPEF signal of *Phycomyces blakesleeanus* hyphae, stained with the vital mitochondrial dye Rhodamine123, excitation wavelength 800 nm, laser power 2 mW, emission filters: VIS (400–700 nm) bandpass filter (from EOS50D camera, Canon), and 530/43 bandpass filter (MF530-43, Thorlabs, Inc.). (**a**) Original, unprocessed image. (**b**) Image deconvoluted using the Richardson–Lucy algorithm in MATLAB software. Deconvolution was performed using the Gaussian distribution with a FWHM equivalent to the FWHM of the PSF measured under identical experimental conditions. The insets show that smaller mitochondria can be resolved when the image is deconvoluted.

resolution. Here, too, significantly poorer results were achieved for the resolution in air.

An interesting observation is that the THG signal of MoS_2 monolayer flakes in glycerin differs from that in air. More specifically, the MoS_2 monolayer flake exhibits a dominant THG signal in glycerin over the substrate-glycerin interface, whereas the same monolayer flake in air suppresses the THG signal. Figure 7a shows the THG signal of MoS_2 immersed in glycerin is presented, whereas Figure 7b demonstrates how the THG signal from the sapphire substrate dominates over the THG signal of the MoS_2 monolayer flake. It is known from the literature that the $\chi^{(3)}$ values of 2DMs depend on the excitation wavelengths (Autere et al., 2018, and references therein; Wang et al., 2013) as well as other parameters such as strain, defects, doping, substrates, and chemical treatment (Autere et al., 2018, and references therein). Here, the only difference between these two systems is the interface, which causes the increase in the nonlinear optical response through phenomenological surface-enhanced THG discussed in Tsang (1995). Although a detailed explanation of this effect is beyond the scope of this discussion, it is worth noting that even in this case, an inverted edge emerges that allows resolution assessment using the knife-edge technique. There is no difference in the assessment of SHG resolution when either material is used.

Image Resolution Improvement by Deconvolution

The PSF full-width values presented in this paper can be used as input data for deconvolution to improve the resolution of images acquired with this NLSM setup. Deconvolution is particularly important for improving image quality when dealing with samples containing structures whose dimensions are very close to the resolution limit, as it enables them to be visualized as distinct and separate objects. Figure 8 shows a representative image before (a) and after (b) deconvolution, highlighting a significant improvement in the efficiency of discerning and identifying small objects within the sample. In Figure 8, the image was deconvoluted using the Richardson–Lucy algorithm in MATLAB software. The deconvolution was performed using a Gaussian distribution with a FWHM equivalent to the FWHM of PSF measured under identical experimental conditions.

Conclusion

We have presented measurements of resolution for all imaging modalities (TPEF, SHG, and THG) of our custom-built NLSM using two distinct approaches. We performed a direct assessment of both lateral (using fluorescent nanospheres in the TPEF modality) and axial resolution (in the SHG and THG modalities). The assessment of lateral resolution in the SHG and THG modalities was performed using the knife-edge technique on WS_2 and MoS_2 monolayers. The lateral technique offers a higher SNR, no photobleaching effect and shows good agreement with the conventional resolution measurement technique using fluorescent nanospheres. Assessing SHG and THG imaging resolution by the knife-edge method overcomes the coherence problem encountered when probing with small (point-like) objects. The obtained results, namely the PSF FWHM values, were employed in image processing by deconvolution, for resolution enhancement.

In addition, we performed a comprehensive analysis of how the resolution varies with numerical aperture of the objective lens, excitation wavelength and refractive index of the embedding medium. The results closest to the theoretical limit were obtained when glycerin was used as the embedding medium at all wavelengths, for both SHG and THG imaging modalities and all objective lenses examined. The latter implies that various embedding media can significantly influence resolution and thus the quality of acquired images. The use of a suitable medium might lead to significantly better imaging results, as objective lenses are usually designed for biological samples embedded in media with a refractive index above 1. As a side note, the intensity of the THG signal from TMD

Downloaded from https://academic.oup.com/mam/advance-article/doi/10.1093/mam/ozae061/7712562 by Dusan Spasojevic user on 12 July 2024

monolayers strongly depends on the substrate- monolayer-medium combination and can either be enhanced or suppressed. For example, MoS_2 monolayer flakes show a pronounced THG signal in glycerin over the substrate-glycerin interface, while the same monolayer flakes in air suppress the THG signal.

In conclusion, the proposed use of WS_2 and MoS_2 monolayers has emerged as a promising tool for the characterization not only of nonlinear imaging systems in terms of lateral and axial resolution, but also of various microscopic systems.

Availability of Data and Materials

The authors have declared that no datasets apply for this piece.

Acknowledgments

We would like to thank Milan Minić for indispensable technical help and support. We thank Professor Michael Pravica from University of Nevada, Las Vegas (UNLV) for reviewing the manuscript.

Author Contributions Statement

J.Z.J. drafted the manuscript, processed the data and reviewed the literature, M.B. performed the measurements, processed the data and reviewed the literature, A.D. sorted out and processed the data and reviewed the literature, A.S. synthesized the MoS_2 monolayer flakes, L.Ž. synthesized the WS_2 monolayer flakes, B.R. performed the PDMS transfer, N.V. supervised the synthesis, T.P. grown the fungi and prepare the sample, M.D.R and A.J.K. built the instrument, performed measurements, processed the data, conceptualized and supervised the research. All authors reviewed the manuscript. J.Z.J., M.B., and A.D. contributed equally to this work. This paper will be the part of midterm check point in their PhD studies.

Financial Support

This research was supported by the Science Fund of the Republic of Serbia, Grant No. 4545, project "Advanced Biophysical Methods for Soil Targeted Fungi-Based Biocontrol Agents" - BioPhysFUN; and the Institute of Physics Belgrade, through the grant by the Ministry of Science, Technological Development and Innovations of the Republic of Serbia. A.S., B.R., and N.V. acknowledge the support of Croatian Science Foundation, Grant No. UIP-2017-05-3869, Centre of Excellence for Advanced Materials and Sensing Devices, ERDF Grant No. KK.01.1.1.01.0001 and Centre for Advanced Laser Techniques, ERDF Grant KK.01.1.1.05.

Conflict of Interest

The authors declare that they have no competing interest.

References

Araújo M, Silva R, Lima E, Pereira D & De Oliveira P (2009). Measurement of Gaussian laser beam radius using the knife-edge technique: Improvement on data analysis. *Appl Opt* **48**, 393–396. https://doi.org/10.1364/AO.48.000393

Autere A, Jussila H, Dai Y, Wang Y, Lipsanen H & Sun Z (2018). Nonlinear optics with 2D layered materials. *Adv Mater* **30**(24), e1705963. https://doi.org/10.1002/adma.201705963

Castellanos-Gomez A, Buscema M, Zant H & Steele G (2013). Deterministic transfer of two-dimensional materials by all-dry viscoelastic stamping. *2D Mater* **1**, 011002. https://doi.org/10.1088/2053-1583/1/1/011002

Chen X, Nadiarynkh O, Plotnikov S & Campagnola P (2012). Second harmonic generation microscopy for quantitative analysis of collagen fibrillar structure. *Nat Protoc* **7**(4), 654–669. https://doi.org/10.1038/nprot.2012.009

Chu S-W, Tai S-P, Ho C-L, Lin C-H & Sun C-K (2005). High-resolution simultaneous three-photon fluorescence and third-harmonic-generation microscopy. *Microsc Res Tech* **66**(4), 193–197. https://doi.org/10.1002/(ISSN)1097-0029

Cole R, Jinadasa T & Brown C (2011). Measuring and interpreting point spread functions to determine confocal microscope resolution and ensure quality control. *Nat Protoc* **6**(12), 1929–1941. https://doi.org/10.1038/nprot.2011.407

Davis B & Brown G (2002). Diffraction by a randomly rough knife edge. *IEEE Trans Antenn Propag* **50**(12), 1769–1778. https://doi.org/10.1109/TAP.2002.804019

Farahi N. (2015). Resolution analysis of films with embedded spheres for imaging of nanoplasmonic arrays. Thesis. ProQuest LLC, Ann Arbor, MI. Available at https://www.proquest.com/openview/bea17cff0074a8c98f01910ec4d90533/1?pq-origsite=gscholar&cbl=18750

Hou R & Labarthet F (2018). Second harmonic generation microscopy from non-centrosymmetric gold half-coated polystyrene spheres. *Surf Sci* **676**, 46–50. https://doi.org/10.1016/j.susc.2018.01.014

Kozubek M (2001). Theoretical versus experimental resolution in optical microscopy. *Microsc Res Tech* **53**(2), 157–166. https://doi.org/10.1002/jemt.1080

Kumar N, Najmaei S, Cui Q, Ceballos F, Ajayan P, Lou J & Zhao H (2013). Second harmonic microscopy of monolayer MoS_2. *Phys Rev B* **87**(16), 161403. https://doi.org/10.1103/PhysRevB.87.161403

Lee G, Jyothsna K, Park J, Lee J, Raghunathan V & Kim H (2023). Confocal nonlinear optical imaging on hexagonal boron nitride nanosheets. *PhotoniX* **4**(1), 27. https://doi.org/10.1186/s43074-023-00103-6

Li Y, Rao Y, Mak K, You Y, Wang S, Dean C & Heinz T (2013). Probing symmetry properties of few-layer MoS_2 and h-BN by optical second-harmonic generation. *Nano Lett* **13**(7), 3329–3333. https://doi.org/10.1021/nl401561r

Mahou P, Malkinson G, Chaudan É., Gacoin T, Beaurepaire E & Supatto W (2017). Metrology of multiphoton microscopes using second harmonic generation nanoprobes. *Small* **13**, 1701442. https://doi.org/10.1002/smll.201701442

Masihzadeh O, Schlup P & Bartels R (2009). Enhanced spatial resolution in third-harmonic microscopy through polarization switching. *Opt Lett* **34**, 1240–1242. https://doi.org/10.1364/OL.34.001240

Masters B & So P (2009). Handbook of biomedical nonlinear optical microscopy. *J Biomed Opt* **14**, 019901. https://doi.org/10.1117/1.3077566

Mehravar S, Cromey B & Kieu K (2020). Characterization of multiphoton microscopes by nonlinear knife-edge technique. *Appl Opt* **59**(22), G219–G224. https://doi.org/10.1364/AO.391881

Mennel L, Furchi MM, Wachter S, Paur M, Polyushkin DK & Mueller T (2018). Optical imaging of strain in two-dimensional crystals. *Nat Commun* **9**(1), 516. https://doi.org/10.1038/s41467-018-02830-y

Mylonakis M, Tserevelakis G, Vlachos G, Fanouraki E, Pavlopoulos A, Pavlidis M & Zacharakis G (2024). Bimodal optical and optoacoustic multiview microscope in the frequency-domain. *Opt Lett* **49**(3), 462–465. https://doi.org/10.1364/OL.510384

Niehues I, Blob A, Stiehm T, Schmidt R, Jadriško V, Radatović B, Čapeta D, Kralj M, Michaelis de Vasconcellos S & Bratschitsch R (2018). Strain transfer across grain boundaries in MoS_2 monolayers grown

Downloaded from https://academic.oup.com/mam/advance-article/doi/10.1093/mam/ozae061/7712562 by Dusan Spasojevic user on 12 July 2024

by chemical vapor deposition. *2D Mater* **5**(3), 031003. https://doi.org/10.1088/2053-1583/aaba9a

Pajić T, Todorovic N, Živić M, Nikolic S, Rabasović M, Clayton A & Krmpot A (2022). Label-free third harmonic generation imaging and quantification of lipid droplets in live filamentous fungi. *Sci Rep* **12**(1), 18760. https://doi.org/10.1038/s41598-022-23502-4

Rabasovic M, Pantelic D, Jelenkovic B, Ćurčić S, Rabasovic M, Vrbica M, Lazovic V, Curcic B & Krmpot A (2015). Nonlinear microscopy of chitin and chitinous structures: A case study of two cave-dwelling insects. *J Biomed Opt* **20**(1), 016010–016010. https://doi.org/10.1117/1.JBO.20.1.016010

Radisavljevic B, Radenovic A, Brivio J, Giacometti V & Kis A (2011). Single-layer MoS_2 transistors. *Nat Nanotechnol* **6**, 147–150. https://doi.org/10.1038/nnano.2010.279

Rigosi AF, Hill HM, Li Y, Chernikov A & Heinz TF (2015). Probing interlayer interactions in transition metal dichalcogenide heterostructures by optical spectroscopy: MoS_2/WS_2 and $MoSe_2/WSe_2$. *Nano Lett* **15**(8), 5033–5038. https://doi.org/10.1021/acs.nanolett.5b01055

Rohrbacher A, Olarte OE, Villamaina V, Loza-Alvarez P & Resan B (2017). Multiphoton imaging with blue-diode-pumped SESAM-modelocked Ti:sapphire oscillator generating 5 nJ 82 fs pulses. *Opt Express* **25**(9), 10677–10684. https://doi.org/10.1364/OE.25.010677

Rosa H, Wei H, Verzhbitskiy I, Rodrigues M, Taniguchi T, Watanabe K, Eda G, Pereira V & Gomes J (2018). Characterization of the second- and third-harmonic optical susceptibilities of atomically thin tungsten diselenide. *Sci Rep* **8**(1), 10035. https://doi.org/10.1038/s41598-018-28374-1

Senkić A, Bajo J, Supina A, Radatović B & Vujičić N (2023). Effects of CVD growth parameters on global and local optical properties of MoS2 monolayers. *Mater Chem Phys* **296**, 127185. https://doi.org/10.1016/j.matchemphys.2022.127185

Squier J & Müller M (2001). High resolution nonlinear microscopy: A review of sources and methods for achieving optimal imaging. *Rev Sci Instrum* **72**(7), 2855–2867. https://doi.org/10.1063/1.1379598

Tsang TY (1995). Optical third-harmonic generation at interfaces. *Phys Rev A* **52**(5), 4116–4125. https://doi.org/10.1103/PhysRevA.52.4116

Tserevelakis G, George F, Krmpot A, Vlachos M, Fotakis C & Tavernarakis N (2010). Imaging *Caenorhabditis elegans* embryogenesis by third-harmonic generation microscopy. *Micron* **41**, 444–447. https://doi.org/10.1016/j.micron.2010.02.006

Tserevelakis G, Psycharakis S, Resan B, Brunner F, Gavgiotakis E, Weingarten K & George F (2012). Femtosecond laser nanosurgery of sub-cellular structures in HeLa cells by employing Third Harmonic Generation imaging modality as diagnostic tool. *J Biophotonics* **5**, 200–207. https://doi.org/10.1002/jbio.201100055

van den Bos A & den Dekker A (2001). Resolution reconsidered-conventional approaches and an alternative. In *Advances in Imaging and Electron Physics*, Peter H (Ed.), vol. **117**, pp. 241–360. Amsterdam: Elsevier.

Wachulak PW, Torrisi A, Bartnik A, Wegrzyński Ł, Fok T & Fiedorowicz H (2017). A desktop extreme ultraviolet microscope based on a compact laser-plasma light source. *Appl Phys B* 123, 1–5. https://doi.org/10.1007/s00340-016-6595-5

Wang R, Chien H-C, Kumar J, Kumar N, Chiu H-Y & Zhao H (2013). Third-harmonic generation in ultrathin films of MoS_2. *ACS Appl Mater Interfaces* **6**(1), 314–318. https://doi.org/10.1021/am4042542

Woodward R, Murray R, Phelan C, Oliveira R, Runcorn T, Kelleher E, Li S, de Oliveira E, Fechine GJM, Eda G & de Matos C (2016). Characterization of the second- and third-order nonlinear optical susceptibilities of monolayer MoS_2 using multiphoton microscopy. *2D Mater* **4**(1), 011006. https://doi.org/10.1088/2053-1583/4/1/011006

Yin X, Ye Z, Chenet D, Ye Y, O'Brien K, Hone J & Zhang X (2014). Edge nonlinear optics on a MoS_2 atomic monolayer. *Science* **344**(6183), 488–490. https://doi.org/10.1126/science.1250564

Zipfel W, Williams R & Webb W (2003). Nonlinear magic: Multiphoton microscopy in the biosciences. *Nat Biotechnol* **21**(11), 1369–1377. https://doi.org/10.1038/nbt899

Downloaded from https://academic.oup.com/mam/advance-article/doi/10.1093/mam/ozae061/7712562 by Dusan Spasojevic user on 12 July 2024

Journal of *Functional Biomaterials*

MDPI

Article

Temperature Sensing Properties of Biocompatible Yb/Er-Doped GdF_3 and YF_3 Mesocrystals

Ivana Dinić [1], Marina Vuković [2], Maria Eugenia Rabanal [3], Milica Milošević [4], Marta Bukumira [5], Nina Tomić [1], Miloš Tomić [1], Lidija Mančić [1,*] and Nenad Ignjatović [1,*]

[1] Institute of Technical Science of SASA, 110000 Belgrade, Serbia; ivana.dinic@itn.sanu.ac.rs (I.D.); nina.tomic@itn.sanu.ac.rs (N.T.); milos.tomic@itn.sanu.ac.rs (M.T.)
[2] Innovative Centre, Faculty of Chemistry, University of Belgrade, 110000 Belgrade, Serbia; marinav@chem.bg.ac.rs
[3] Department of Materials Science and Engineering and Chemical Engineering, Universidad Carlos III de Madrid and IAAB, 28903 Madrid, Spain; eugenia@ing.uc3m.es
[4] Department of Radiation Chemistry and Physics, Vinča Institute of Nuclear Sciences—National Institute of the Republic of Serbia, University of Belgrade, Vinča, 110000 Belgrade, Serbia; milicam@vin.bg.ac.rs
[5] Institute of Physics Belgrade, National Institute of the Republic of Serbia, University of Belgrade, 110000 Belgrade, Serbia; marta@ipb.ac.rs
* Correspondence: lidija.mancic@itn.sanu.ac.rs (L.M.); nenad.ignjatovic@itn.sanu.ac.rs (N.I.)

Abstract: $Y_{0.8-x}Gd_xF_3$:Yb/Er mesocrystals with a biocompatible surface and diverse morphological characteristics were successfully synthesized using chitosan-assisted solvothermal processing. Their structural properties, studied using X-ray powder diffraction, Fourier transform infrared spectroscopy, scanning and transmission electron microscopy and energy dispersive X-ray analysis, were further correlated with the up-conversion emission (λ_{exc} = 976 nm) recorded in function of temperature. Based on the change in the visible green emissions originating from the thermally coupled $^2H_{11/2}$ and $^4S_{3/2}$ levels of Er^{3+}, the corresponding LIR was acquired in the physiologically relevant range of temperatures (25–50 °C). The detected absolute sensitivity of about 0.0042 $°C^{-1}$, along with the low cytotoxicity toward both normal human lung fibroblasts (MRC-5) and cancerous lung epithelial (A549) cells, indicate a potential for use in temperature sensing in biomedicine. Additionally, their enhanced internalization in cells, without suppression of cell viability, enabled in vitro labeling of cancer and healthy cells upon 976 nm laser irradiation.

Keywords: optical thermometry; up-conversion; YF_3; GdF_3; chitosan; mesocrystals; cytotoxicity

check for updates

Citation: Dinić, I.; Vuković, M.; Rabanal, M.E.; Milošević, M.; Bukumira, M.; Tomić, N.; Tomić, M.; Mančić, L.; Ignjatović, N. Temperature Sensing Properties of Biocompatible Yb/Er-Doped GdF_3 and YF_3 Mesocrystals. *J. Funct. Biomater.* **2024**, *15*, 6. https://doi.org/10.3390/jfb15010006

Received: 15 November 2023
Revised: 15 December 2023
Accepted: 20 December 2023
Published: 22 December 2023

Copyright: © 2023 by the authors. Licensee MDPI, Basel, Switzerland. This article is an open access article distributed under the terms and conditions of the Creative Commons Attribution (CC BY) license (https://creativecommons.org/licenses/by/4.0/).

1. Introduction

Lanthanide doped up-conversion nanoparticles (Ln-UCNPs) belong to the photoluminescence materials whose optical activity, known as the anti-Stokes emission, is described as a nonlinear optical process of the successive absorption of two or more photons, and the emission of light with a shorter wavelength than the excitation one [1]. Their UC luminescence, superior to that of the transition metal ions doped counterparts, is based on the unique electronic configuration of lanthanide ions, $4f^n5s^25p^66s^2$ (n = 0–14). All lanthanides, with the exception of ytterbium and cerium, have abundant ladder-like 4f energy levels, with electrons having a low electron-phonon coupling strength due to the shielding from the outer-lying $5s^2$ and $5p^6$ levels. With the removal of $6s^2$ electrons, 4f electrons become optically active, either through 4f or 4f-5d transitions [2]. Among lanthanides, Er^{3+}, Ho^{3+} and Tm^{3+} are considered to be the most effective activators [3], while Yb^{3+} is recognized as an ideal sensitizer, due to its simple energy level and a relatively high cross-section for absorption at 980 nm. When co-doped together in different host materials with a low phonon energy (~350 cm^{-1}), broad band gap (>10 eV) and high chemical stability, these emit intense blue, green or red light under near-infrared (NIR) excitation. At present, the

Ln-UCNPs emission covers the whole visible spectrum. Accordingly, Ln-UCNPs have potential application in biomedicine for cell labeling or as theranostic agents, in forensics for latent fingerprint visualization, and in security applications for anti-counterfeiting [3–5]. Their innovative use in photovoltaic, agriculture and thermal sensing in medicine has recently been in the focus of scientific research [6–8]. In particular, temperature sensing, which relies on change in the luminescence intensity ratio (LIR) of thermally coupled energy levels of lanthanide ions, is highly sensitive, self-referenced and does not require additional calibration. LIR-based thermometers are negligibly dependent on the extrinsic factors and could be used for non-contact temperature measurements in diverse areas and environments. To date, many different Ln-UCNPs are explored for this purpose. In addition to the most efficient hexagonal $NaYF_4$:Yb/Er phase, Ln-doped $NaGdF_4$, YF_3, Y_2O_3, $Y_6O_5F_8$, $Ba_3Gd_2F_{12}$ and $Y_3Al_5O_{12}$ are reported to have excellent temperature sensing capability, even when embedded in glass [9–14]. In order to be useful for in vivo temperature sensing and photothermal therapy, Ln-UCNPs need to have a hydrophilic, biocompatible surface, and need to be sensitive in the physiologically relevant range of temperatures. The required surface features are usually ensured through subsequent coating with SiO_2 or a biocompatible polymeric shell [15]. Another effective approach is in situ capping of UCNPs with amino or carboxylic functional groups during synthesis [16]. As we showed in our previous work, chitosan and poly lactic-co-glycolic acid used in the hydrothermal synthesis of $NaYF_4$:Yb/Er provides sufficient hydrophilicity and biocompatibility of UCNPs without affecting their luminescence efficiency and cell labeling capacity [17,18]. A similar synthesis approach is used in the present study for obtaining $Y_{1-x}Gd_xF_3$:Yb/Er UCNPs with a biocompatible surface. Er^{3+} is the most commonly used lanthanide ion for LIR-based thermometry in the physiologically relevant range of temperatures due to the outstanding thermal coupling between $^2H_{11/2}$ and $^4S_{3/2}$ energy levels, which is separated by ca. 750 cm^{-1}. While the maximal thermal sensitivity (S) of ~1%K^{-1} is determined for YF_3:Yb/Er UCNPs at 293 K [19,20], there is no data evidencing the thermal sensing capacity of GdF_3:Yb/Er UCNPs. It is shown that along with NIR bio-imaging and enhanced photodynamic therapy [21], gadolinium-based UCNPs additionally provide a positive contrast effect in T1-weighted magnetic resonance imaging. Accordingly, they could be used as dual modality imaging agent biolabels [22]. Hence, the LIR-based temperature sensitivity and potential cytotoxicity of both, GdF_3:Yb/Er and YF_3:Yb/Er particles synthetized via chitosan assisted solvothermal synthesis, were investigated in this study.

2. Materials and Methods

2.1. Materials

All reagents were purchased from Sigma–Aldrich (St. Louis, MO United States) and used as obtained. Rare earth (RE) nitrates [$Y(NO_3)_3 \times 6H_2O$, $Gd(NO_3)_3 \times 6H_2O$, $Yb(NO_3)_3 \times 5H_2O$ and $Er(NO_3)_3 \times 5H_2O$], sodium fluoride (NaF, ≥99%), anhydrous ethylene glycol ($C_2H_6O_2$, 99.8%) and chitosan (CS, low molecular weight, 50,000–190,000 Da) were used for $Y_{0.8-x}Gd_xF_3$:$Yb_{0.18}Er_{0.02}$ particles synthesis (x = 0, 0.15 and 0.8). In addition to the variation in the gadolinium content, two concentrations of the precursor solution were used for the synthesis of $Gd_{0.8}F_3$:Yb/Er, low ($C_{RE}{}^{3+}$: 2.5 mmol, CS: 50 mg) and high ($C_{RE}{}^{3+}$: 5 mmol, CS: 100 mg), so samples are marked as shown in Table 1.

Table 1. Composition of samples and precursors.

Nominal Composition	Sample Name	$C_{RE}{}^{3+}$ (mmol)	CS (mg)
$Y_{0.8}F_3$:$Yb_{0.18}Er_{0.02}$	YF-L	2.5	50
$Y_{0.65}Gd_{0.15}F_3$:$Yb_{0.18}Er_{0.02}$	YGF-L	2.5	50
$Gd_{0.8}F_3$:$Yb_{0.18}Er_{0.02}$	GF-L	2.5	50
$Gd_{0.8}F_3$:$Yb_{0.18}Er_{0.02}$	GF-H	5	100

2.2. Synthesis of $Y_{1-x}Gd_xF_3$:Yb,Er Particles

Up-converting particles with a nominal compositions $Y_{0.8}F_3$:$Yb_{0.18}Er_{0.02}$, $Y_{0.65}Gd_{0.15}F_3$:$Yb_{0.18}Er_{0.02}$ and $Gd_{0.8}F_3$:$Yb_{0.18}Er_{0.02}$ were solvothermally synthetized in the presence of chitosan using the following precursor: RE-nitrates were dissolved in 10 mL of deionized water and mixed with 15mL of the chitosan solution; then, 10 mL of the NaF solution (F^+/RE^{3+} = 7) and 35 mL of ethylene glycol were added; the obtained precursor was stirred for 20 min. The synthesis was performed with constant stirring (100 rpm) in a sealed PTFE linen autoclave at 200 °C for 2 h. After cooling, the product of the reaction was separated through centrifugation (8000 rpm), rinsed with ethanol and water several times, and dried at 90 °C (2 h).

2.3. Characterization

The phase composition of the samples was examined using X-ray powder diffraction (XRPD) at room temperature, using a Rigaku SmartLab diffractometer (Rigaku Europe, Neu-Isenburg, Germany) with CuKα radiation and the 2θ scanning rate of 0.01°/s. The structural data for the powders were acquired through LeBail and Rietveld refinement in Topas 4.2 (Bruker AXS GmbH, Karlsruhe, Germany) [23]. The morphology, particle size, and chemical composition were examined using a scanning electron microscope (SEM, Philips XL 30/EDAX-Dx4, Philips, Amsterdam, Netherlands) equipped with an energy dispersive X-ray detector (EDS). Transmission electron microscopy (TEM) combined with the selected area electron diffraction (SAED) study was performed on a JEOL JEM 2100 instrument (JEOL, Akishima, Tokyo, Japan) operated at an accelerating voltage of 200 kV. Prior to this, the samples had been ultrasonically dispersed in acetone and deposited on a holey carbon copper grid. DigitalMicrograph™ (DM, Gatan Inc., 3.7.4, Pleasanton, CA, USA) software was used for phase identification based on the fast Fourier transform (FFT) calculation of an image. The SEM images were used to analyze the particle size distribution. For every sample, the dimensions of at least 50 particles chosen randomly were measured. Fourier transform infrared spectroscopy (FTIR) was performed using a Nicolet iS10 FT-IR Spectrometer (Thermo Scientific Instruments, San Diego, CA, USA) in the spectral range from 400 to 4000 cm^{-1}. Photoluminescence (PL) emission measurements were performed at room temperature using a TE-cooled CCD fluorescence spectrometer (Glacier X, BWTEK, Plainsboro, NJ, USA) and a 976 nm laser diode (single mode pigtailed BL976-SAG300 laser diode of 976 nm, Thorlabs, Newton, NJ, USA). For temperature-dependent measurements of PL intensity, a Peltier element (20 × 20 mm) was used along with the PID temperature controller (Wavelength electronics WTC32ND-EV, Wavelength electronics Inc., Bozeman, MT, USA) in the temperature range from 25 to 50 °C. The temperature of the upper surface of the element, on which the sample was placed, was measured using a 10 kΩ thermistor, bonded to the surface. The set temperature was maintained with the stability of 0.002 °C. In order to avoid the local heating of the sample, the excitation was performed via laser radiation in very short pulses of 10 ms, with frequency of 1 Hz, giving a fill factor of 1:100. The luminescent radiation was collected using a multimode optical fiber with a large diameter (0.6 mm) and a large numerical aperture (0.22), and further introduced into the spectrum analyzer. All spectrograms were recorded without pulse averaging and were fitted with 5 separate Gaussian spectral lines, and appropriate integrals were used to find the LIR.

2.4. Cell Lines

Human cells used for the testing of cytotoxic effects were ATCC cell lines MRC-5 (ECACC 84101801) and A549 (ATCC CCL-185). MRC-5 cells are normal human lung fibroblasts, used as a general model in routine testing for cytotoxicity, even for testing medical devices, as recommended by ISO 10993-5:2009(E) [24]. The A549 cell line is a line of cancerous lung epithelial cells, chosen as a model for testing the influence on lung epithelial cells, and also as a supplementary model for assessing the effect of materials on different cell types. The cells of both lines were maintained in Dulbecco's Modified Eagle Medium

with L-glutamine, supplemented with 10% of fetal bovine serum and 100 U/mL of the penicillin/streptomycin mix, in a humidified atmosphere at 37 °C and 5% CO_2. The cell medium was changed every 2 days. Cells were passaged before reaching 80% confluency, using trypsinization with 0.1% trypsin/EDTA.

2.5. Cell Viability Assay

For assessing the cytotoxic effect of the samples, an MTT colorimetric assay was performed. Cells (2×10^4 cells/well) were seeded in 96 well plates, followed by incubation at 37 °C and 5% CO_2 for 24 h. The medium was then discarded, and cells were exposed to three different concentrations (10, 25 and 50 μg/mL) of the samples. Prior to addition to the wells, the test samples were dispersed in the cell media, followed by vortex (3 × 1 min) and ultrasonic dispersion for 3 min, to obtain suspensions. After 24 h of incubation under the same conditions, the treatment medium was removed, and cells were carefully washed using 1x phosphate buffered saline. FA fresh medium with 0.5 mg/mL of MTT dye (3-[4,5-dimethylthiazol-2-yl]-2,5-diphenyltetrazolium bromide) was then added and plates were incubated for another 3 h, allowing for the formation of formazan crystals. After the removal of the medium containing MTT, crystals were dissolved using DMSO and by shaking the plate. Absorbance was recorded at 570 nm using a Multiskan plate reader (Thermo Scientific Instruments, San Diego, CA, USA) and average survival was calculated comparing the absorbance levels in treated cells with absorbance of non-treated, control groups.

2.6. Cell Imaging by Laser Scanning Microscopy

For the visualization of GF-L uptake by A549 cells 50 μg mL^{-1} of sterile suspension was filtered through 0.45 μm syringe filter to separate agglomerates that could provoke saturation during imaging. Coverslips were cut into 8 × 8 mm square pieces and sterilized by using ethanol and UV light. Then, they were placed at the bottom of 12 well plates. Cells were trypsinized from flasks in which they were grown and seeded to the wells at the density of 105 cells/mL. After seeding, cells were incubated for 24 h at 37 °C and 5% CO_2 to allow attachment and proliferation. The medium was then replaced with the fresh medium containing 50 μg/mL of GF-L nanoparticles, and plates incubated for another 24 h with the treatment, at the same conditions. On the third day, cells were gently washed for three times by using pre-warmed 1 × PBS, in order to wash out the remaining unbonded mesocrystals. An amount of 4% paraformaldehyde was applied for 20 min to allow the fixation of the cells. Then it was thoroughly washed with 1xPBS several times. Coverslips containing fixated cells were removed from the wells and placed with the cell-covered side facing down to the 20 μL drops of Mowiol on the microscopic slides. Samples were then left to dry on the ambient temperature for 24 h before they were observed under laser scanning microscopy.

Two-photon excited (auto)fluorescence of A549 cells and the up-conversion of GF-L mesocrystals were recorded using a custom made nonlinear laser scanning microscope with the excitation wavelengths of 730 nm and 976 nm, respectively. Microscope set-up description is given elsewhere [17,18]. The signal was collected in back reflection, using an oil immersion objective lens with high a numerical aperture (EC Plan-NEOFLUAR, NA = 1.3; Carl Zeiss AG, Oberkochen, Baden-Württemberg, Germany). A visible wide range bandpass filter (400–700 nm) was used to filter out the laser and transmit only the signal. Obtained raw data was processed and analyzed using ImageJ software (1.47v, National Institutes of Health, Bethesda, MD, USA).

2.7. Assessment of the Cell Morphology Parameters and Fluorescence

Cell morphology in culture was inspected via bright field microscopy before and after the addition of treatment and during the incubation time. From the images obtained using the laser scanning microscope, cell morphology parameters were assessed as follows, cell

size, in terms of cell diameter, surface and nucleus/cytoplasmic ratio. Nuclear circularity index was also calculated, as described in [25], using the Equation (1):

$$\text{Circularity} = \frac{4\pi \times \text{area}}{(\text{perimeter})^2} \quad (1)$$

To roughly estimate the amount GF-L mesocrystals association with different cells, average fluorescence per cell was assessed by measuring the pixel intensity from the laser microscopy images of MRC-5 and A549 with filtered fluorescence originating by GF-L mesocrystals. All measurements were performed by using ImageJ software.

2.8. Statistical Analysis

All cell viability tests were performed in triplicate, and in three independent experiments. The results of the viability of the treated cells were compared to the average absorbance of untreated control cells, and are presented in diagrams as the average values of the percent of survival, +/− standard deviation. Experimental and control groups were compared depending on the number of samples via Student's *t*-test or one-way analysis of variance (ANOVA), followed by Tukey's post hoc test, with p value being set to $p < 0.05$.

3. Results

The XRPD patterns, presented at Figure 1a. indicate that all samples crystallize in the β-YF_3 type orthorhombic crystal structure (S.G. *Pnma*), JCPDS 01-074-0911. In this structure, the Y^{3+} ion is coordinated by nine F^- ions. Its substitution by Gd^{3+}, which has a larger ionic radius (Gd^{3+}:1.107 Å, Y^{3+}:1.075 Å), led to an increase in crystal lattice parameters, due to which, the shifting of the (020), (111), (210) and (121) reflections towards lower values of 2Θ is notable, Figure 1b. The XRPD structural refinement (Figure 1c,d, Table 2), reveals the coexistence of two different particle populations in all samples (two phases of the same composition were used to adjust the experimental pattern), both adopting the same *Pnma* space group with similar unit cell parameters and a quite different crystallite size and strain. The smallest difference in the crystallite sizes of two populations was detected in the GdF-L sample, where both values were below 100 nm, Table 2.

Table 2. Refined microstructural parameters of $Y_{1-x}Gd_xF_3$:Yb/Er samples.

Sample	Unit Cell Parameters (Å)			CS (nm)	Strain	R_{Bragg}
	a	b	c			
YF-L	6.2926 (3)	6.8621 (3)	4.4984 (3)	207 (23)	0.323 (5)	1.1
	6.3098 (5)	6.8605 (5)	4.4400 (5)	18 (1)	0.130 (1)	1.3
YGF-L	6.3331 (5)	6.8749 (5)	4.4453 (5)	20 (1)	0.120 (1)	1.6
	6.3239 (5)	6.8713 (5)	4.5050 (2)	183 (10)	0.280 (2)	2.2
GF-L	6.4685 (4)	6.9586 (4)	4.4604 (4)	23 (1)	0.174 (6)	1.1
	6.4590 (4)	6.9565 (4)	4.4011 (4)	64 (2)	-	2.5
GF-H	6.4751 (4)	6.9490 (3)	4.4256 (8)	120 (6)	0.195 (3)	1.4
	6.4885 (2)	6.9602 (2)	4.4318 (1)	37 (1)	-	1.7

The size and the morphology of the synthetized particles were revealed by (SEM and TEM. The particles obtained from the precursors with a low concentration have an elongated shape similar to unshelled peanuts, the length of which decreases from 1 μm to 300 nm as the gadolinium content increases, Figure 2. The particles appear to be non-agglomerated and quite uniform in size. As observed in Figure 2, they are composed of smaller nanocrystals and are porous to a certain degree. Their high purity and the uniform distribution of all constituting elements (yttrium: Kα at 14.931 and Lα at 1.92 keV; ytterbium: Lα at 7.414 and Mα at 1.404 keV; erbium: Lα at 6.949 and Mα at 1.521 keV;

gadolinium; Kα at 6.053 and Mα at 1.181 keV; and fluorine: Kα at 0.677), are confirmed by EDS elemental mapping, Figure 3.

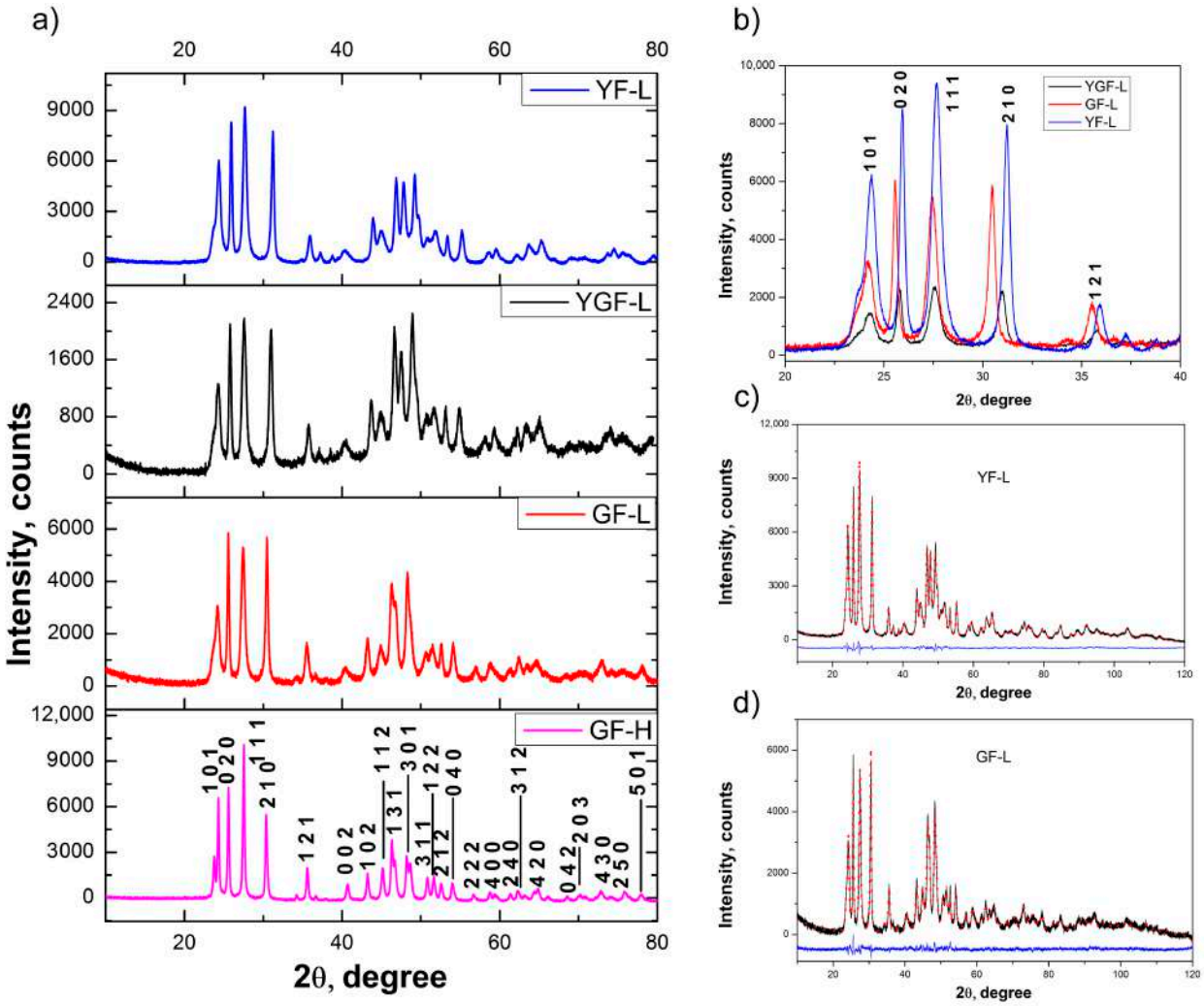

Figure 1. XRPD patterns of $Y_{0.8-x}Gd_xF_3$:$Yb_{0.18}Er_{0.02}$ samples (**a**) reflection shifting due to Gd^{3+} content increase (**b**) and Rietveld refinement of samples YF-L and GF-L (**c**,**d**). In (**b**–**d**) the experimental data are shown as the black solid line while the red dotted pattern corresponds to the calculated data. The differences between the observed and calculated intensities are plotted in the blue line.

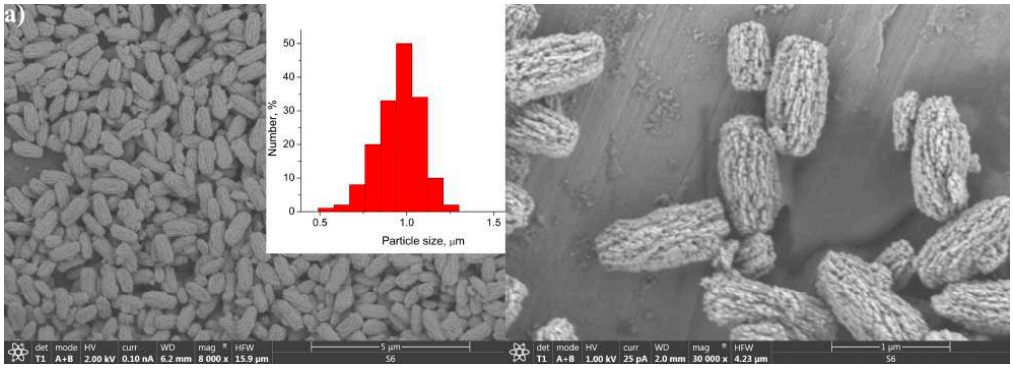

Figure 2. *Cont.*

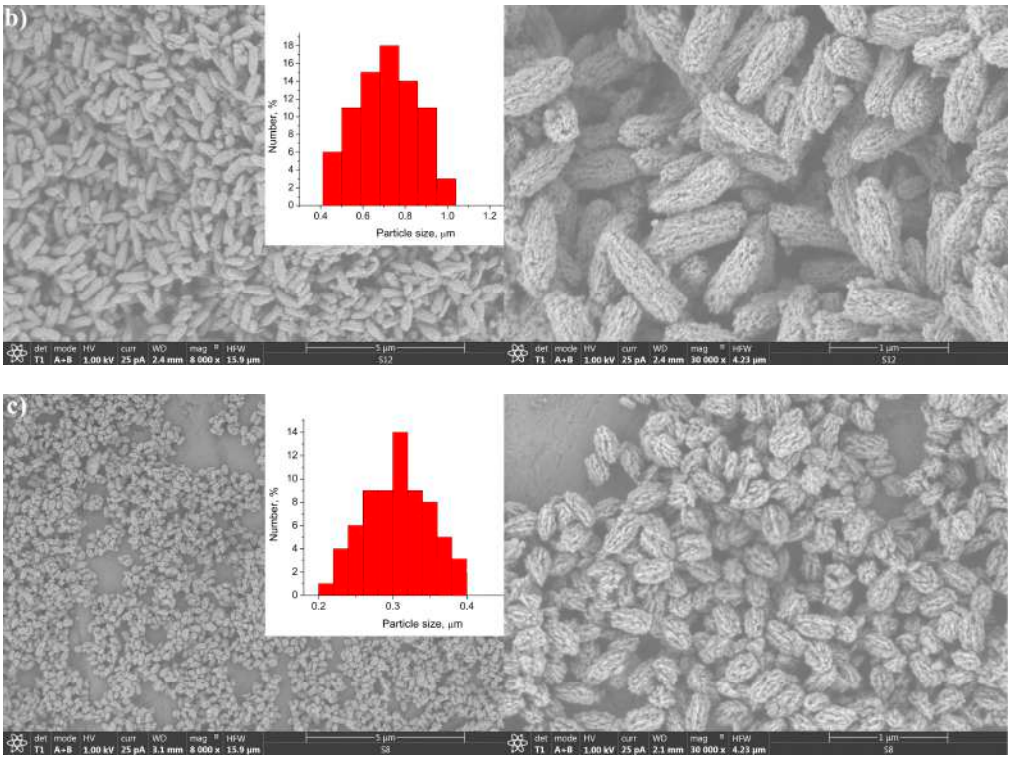

Figure 2. SEM of the samples YF-L (**a**), YGF-L (**b**), and GF-L(**c**), with the corresponding particle size distribution**.**

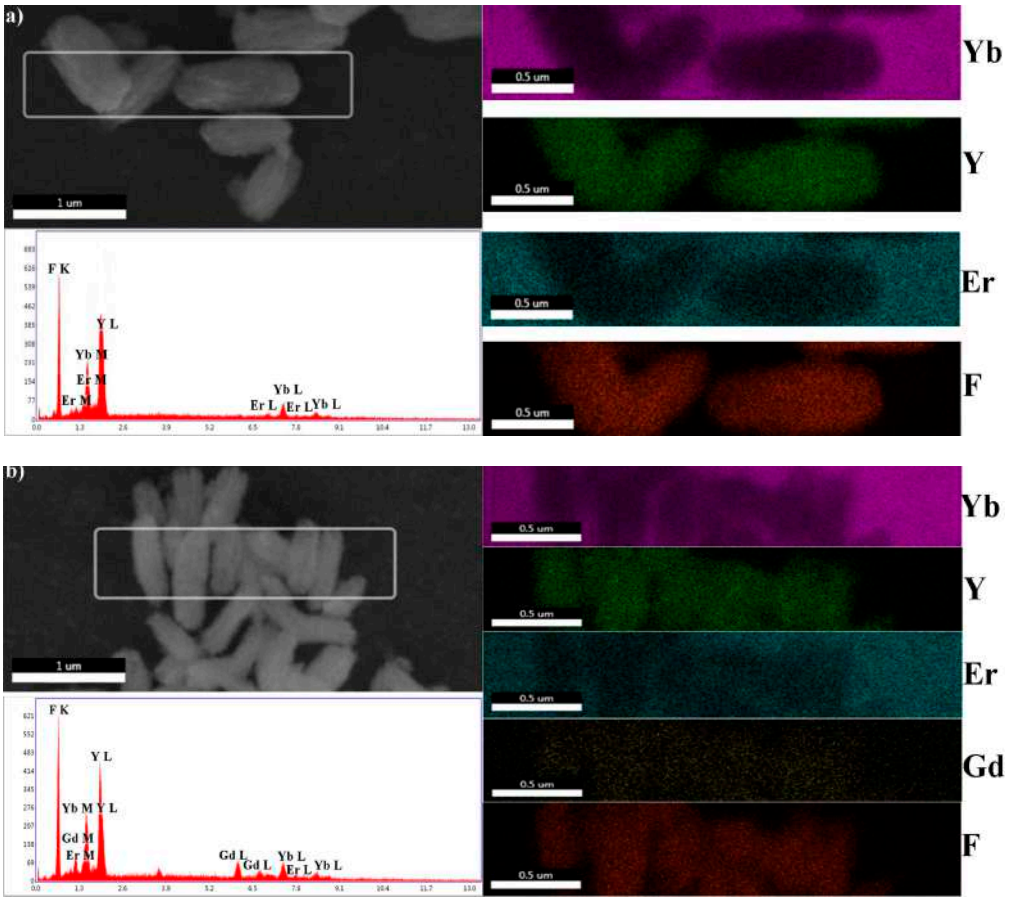

Figure 3. *Cont*.

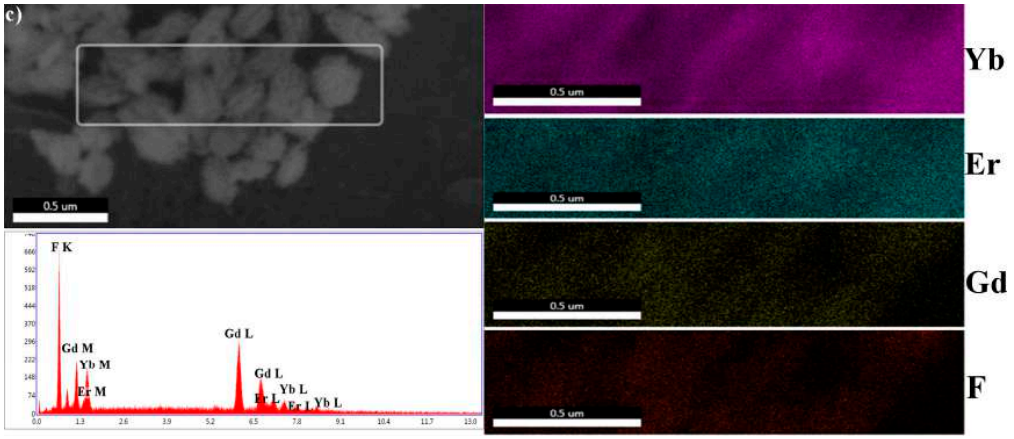

Figure 3. EDS analyses of the samples YF-L (**a**), YGF-L (**b**), and GF-L (**c**).

The TEM analysis of the YF-L and Gd-L samples confirms that the unshelled peanuts -shaped particles are mesocrystals formed by much smaller monocrystals, Figures 4 and 5. The shape of these monocrystals is slightly elongated in the YF-L particles. As evident in Figure 4b, they are self-assembled to form rice-shaped mesocrystals by attaching to each other along the longer edge. The development of moiré fringes, visible in Figure 4c, suggests the internal displacement of crystal planes in elongated nanocrystals due to the lattice defects. The SAED pattern, Figure 4d, shows indexed diffraction rings of (111), (210), (311) and (321) crystal planes with d values of 3.20 Å, 2.85 Å, 1.80 Å and 1.60 Å, respectively. All values align well with corresponding ones from the JCPDS 01-074-0911 card. The GdF-L mesocrystals are composed of smaller quasi-spherical nanocrystals. Figure 5c, reveals the presence of (111) crystallographic planes of gadolinium fluoride. In addition, the monophase composition of particles is identified by the presence of the (111), (201), (112), (122) and (240) planes with d values corresponding well to those obtained through the XRPD analysis.

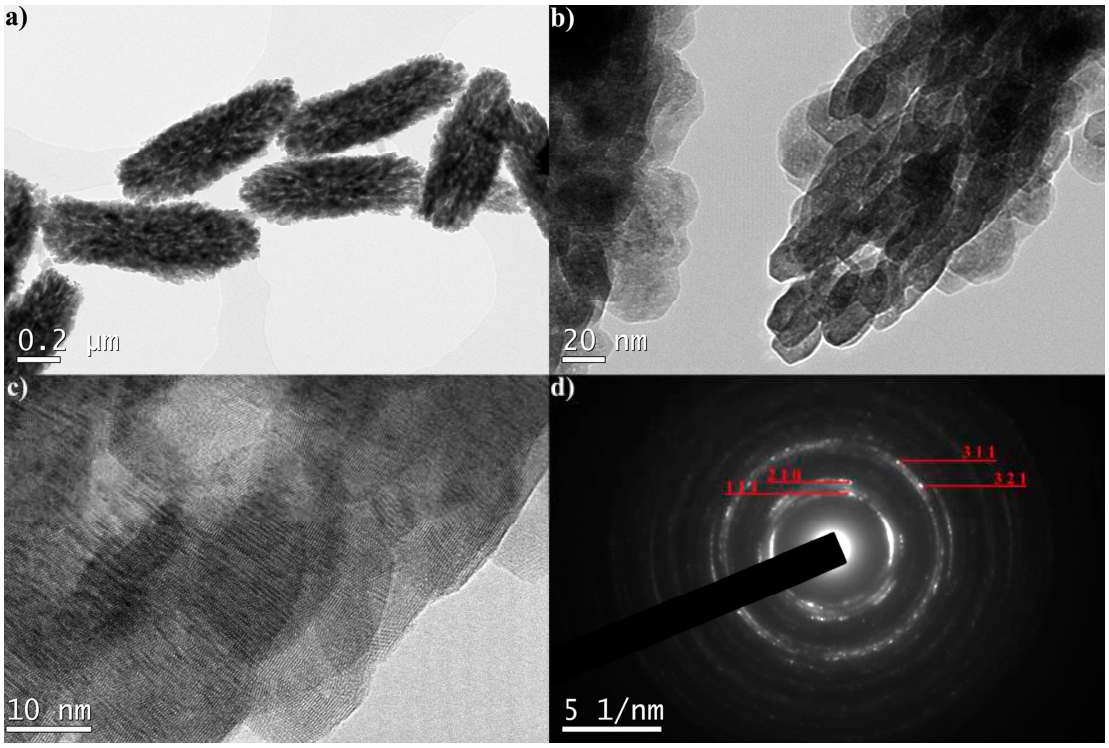

Figure 4. TEM images (**a**–**c**) and SAED pattern of YF-L mesocrystals (**d**).

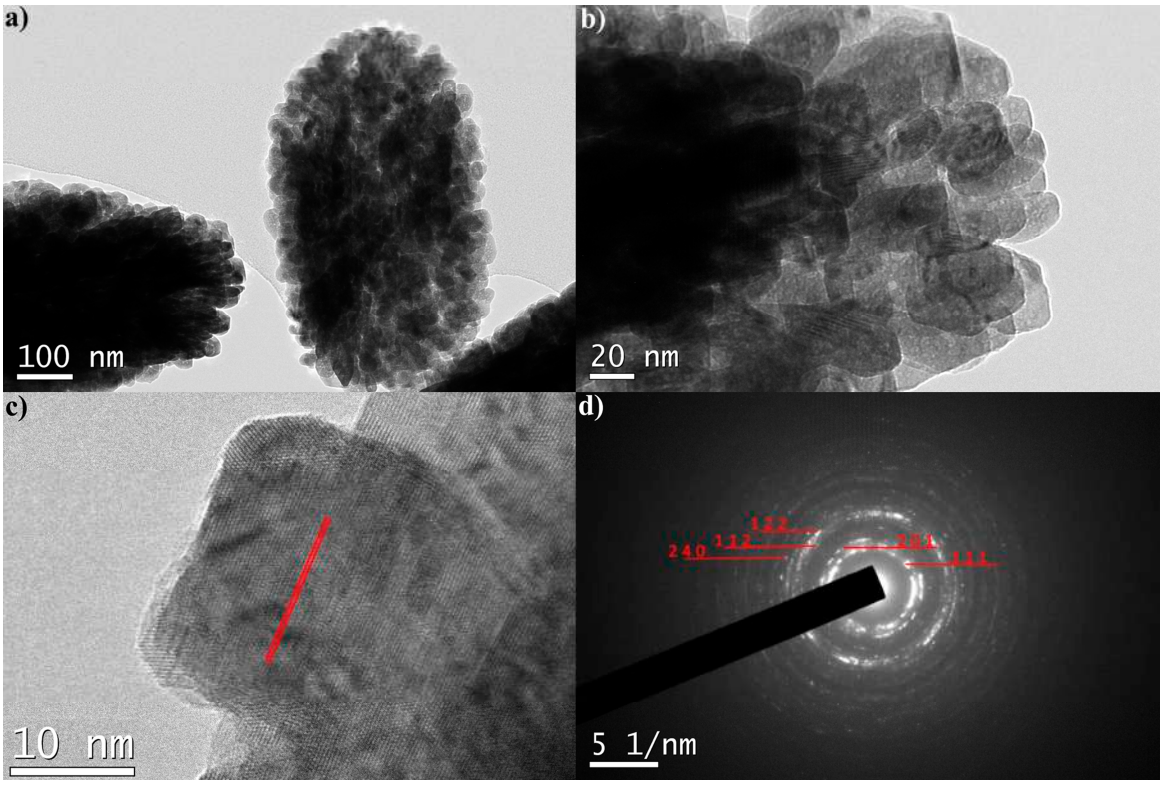

Figure 5. TEM images (**a**–**c**) and SAED pattern of GF-L mesocrystals (**d**). Red lines in (**c**) indicate crystal planes.

With the increased precursor concentration, a change in the particles' morphology was detected. The formation of rhombic mesocrystals with a layered structure, and the diagonal length up to 0.4 μm, were revealed by the SEM analysis, Figure 6a,b. They are built by orientational ordering and layering of thin plates, Figure 6c. As it is notable from the TEM image shown in Figure 6e, the formation of plates is effectively guided by the oriented attachment of rod-like $Gd_{0.8}F_3$:$Yb_{0.18}Er_{0.02}$ monocrystals whose indexed diffraction spots are given in Figure 6f.

The Fourier transform infrared (FTIR) spectra of the synthetized samples and pure chitosan presented in Figure 7, indicate the preservation of chitosan ligands onto the surface of mesocrystals. According to the literature data [26–28], the spectrum of pure chitosan can be classified as follows: broad band at 3500–3000 cm^{-1} (stretching vibration of hydroxyl O-H which overlaps with amine N-H group); band at 2870 cm^{-1} (C-H bond in $–CH_3$); bands at 1651.7 cm^{-1} and 1587 cm^{-1} (C=O stretching (amide I) and NH stretching (amide II), respectively); bands at 1417.9 cm^{-1} and 1374.1 cm^{-1}(CH_3 bending vibrations); band at 1149.9 cm^{-1} (asymmetric vibration of the CO group); a band near 1060.2 cm^{-1} (CO bending vibrations of the pyranose ring). The FTIR spectrum of the samples showed a decrease in adsorption and a slight shifting of chitosan related bands at: 3399.9 cm^{-1} (-OH and amine -NH group stretching), 1651.7 cm^{-1} (C=O stretching), 1557 cm^{-1} (protonated amine stretching), 1373.5 cm^{-1} (CH_2 bending) and 1080.4 cm^{-1} (CO bending), implying its preservation at the particles surface.

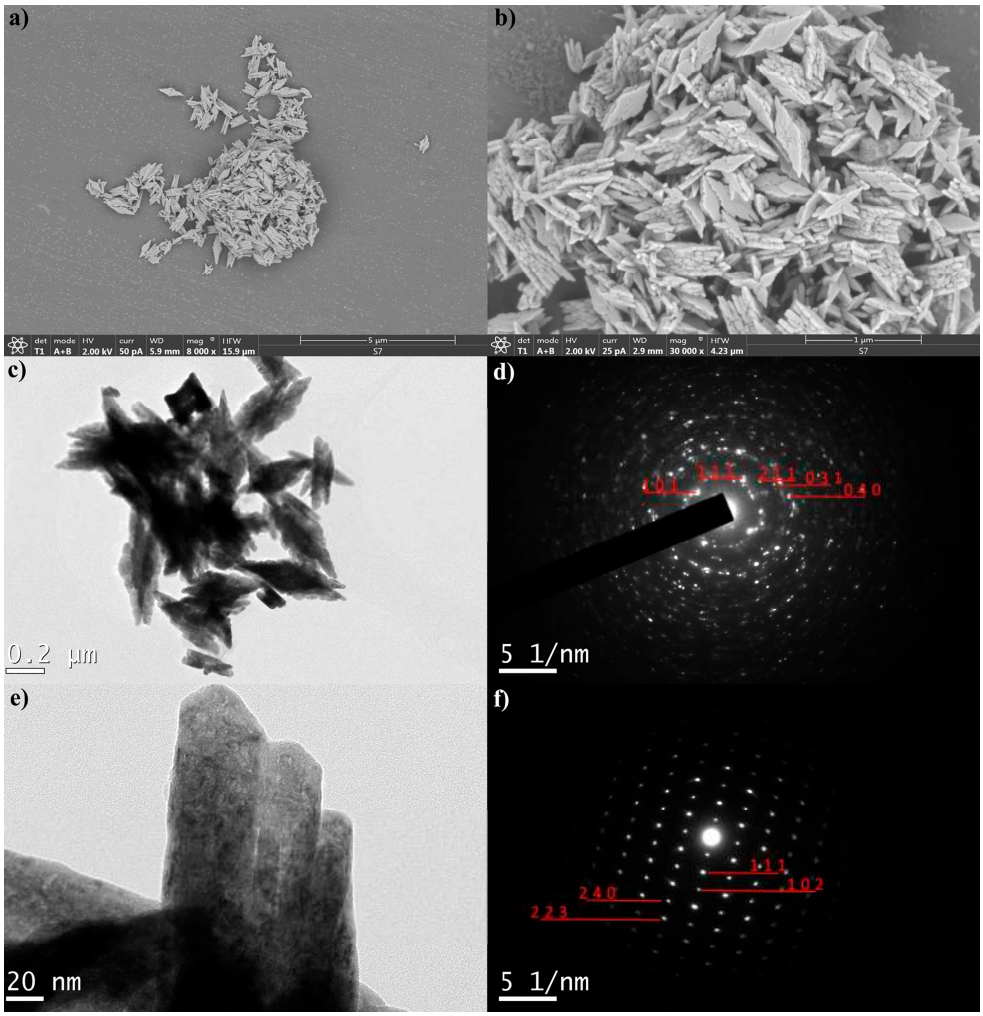

Figure 6. SEM (**a**,**b**) and TEM (**c**,**e**) and SAED images (**d**,**f**) of GF-H sample.

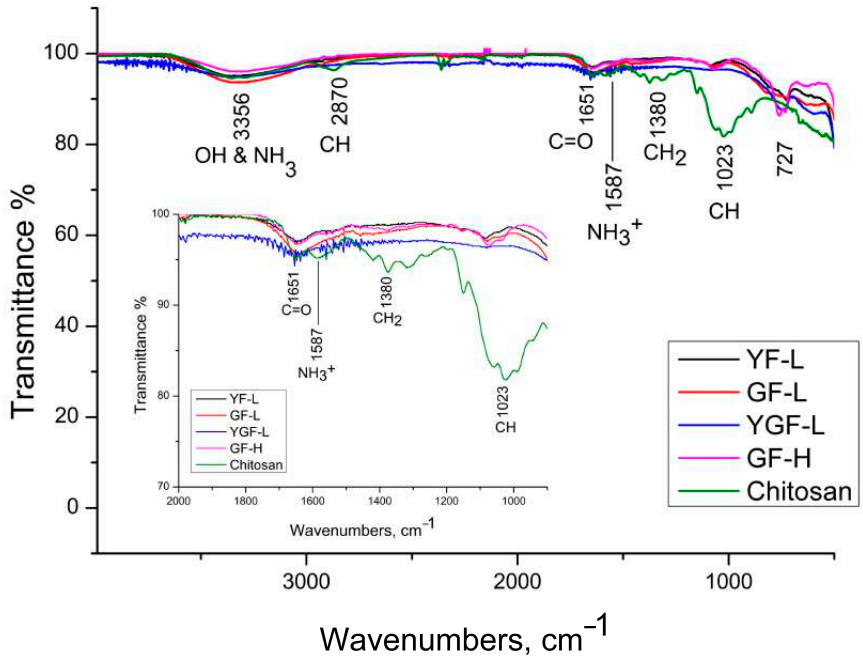

Figure 7. FTIR spectrum of samples and pure chitosan.

The viability of the MRC-5 and A549 cells exposed to the concentrations of 10, 25 and 50 µg/mL of YF-L and GF-L samples for 24 h, expressed as percentages of the control cells viability, are shown in Figure 8. As observed from the graphs, all cells treated exhibited more than 80% viability, at all concentrations of both samples. The cell viability was highly preserved after a 24-h exposure, being above 80% for all examined concentrations of both samples. There was a negligible difference between the groups treated with various concentrations of GF-L, where no concentration dependency was observed. On the other hand, the viability of A549 treated with YF-L at the concentration of 25 µg/mL, was found to be slightly reduced compared to the viability of MRC-5 cells (at the same concentration). These results confirm that both samples are outstandingly biocompatible with human cells.

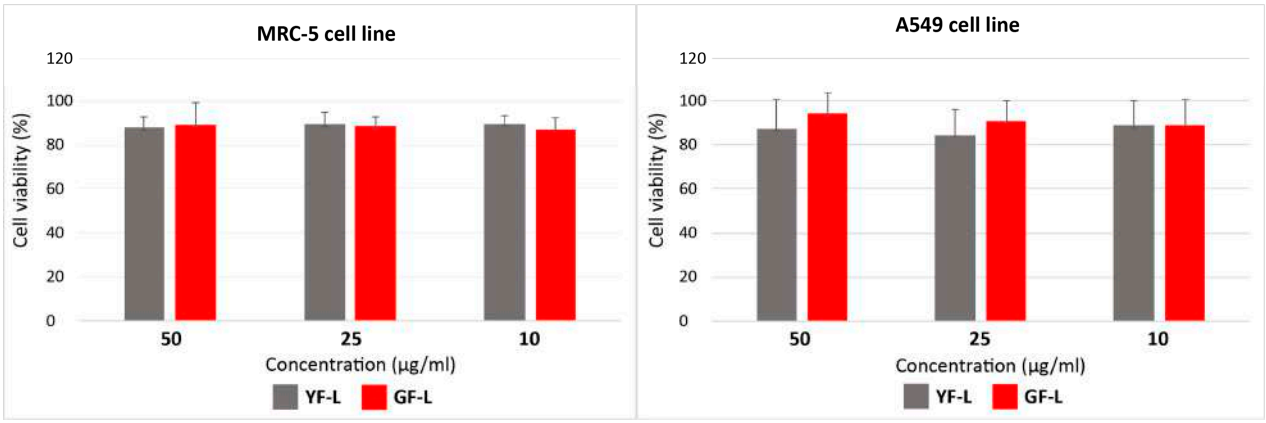

Figure 8. Cytotoxicity assay of YF-L and GF-L samples in MRC-5 and A549 after a 24-h exposure.

Figure 9a shows the UC emission spectra of all samples under 976 nm excitation. The visible emissions from $^2H_{9/2} \rightarrow {}^4I_{15/2}$, $^4F_{7/2} \rightarrow {}^4I_{15/2}$, $^2H_{11/2}$,$^4S_{3/2} \rightarrow {}^4I_{15/2}$, and $^4F_{9/2} \rightarrow {}^4I_{15/2}$, transitions of Er^{3+} ions were detected at 409, 488, 520/550, and 659 nm, respectively. As shown in Figure 9b, the population of the excited states in Er^{3+} ions are due to energy transfer from the Yb^{3+} sensitizer. Initially, Yb^{3+} ions were excited from the $^2F_{7/2}$ ground state to the $^2F_{5/2}$ excited state through the absorption of the incident photons. This energy is transferred further to the $^4I_{11/2}$ state of the Er^{3+} ion. The population of the $^4I_{11/2}$ state also occurs through the direct excitation of Er^{3+} ions from their ground $^4I_{15/2}$ state. The population of the higher $^4F_{7/2}$ and $^4F_{9/2}$ Er^{3+} levels occurs either through energy transfer from another excited Er^{3+} ion which is in close proximity, or through a two-step energy transfer from Yb^{3+} to the neighboring Er^{3+} ions. The populated $^4F_{7/2}$ state of Er^{3+} ions relax radiatively to the ground $^4I_{15/2}$ state or non-radiatively decay to the $^2H_{11/2}$ and $^4S_{3/2}$ states, from which radiative de-excitations to the ground $^4I_{15/2}$ state generate green emission at 520 nm ($^2H_{11/2} \rightarrow {}^4I_{15/2}$) and 550 nm ($^4S_{3/2} \rightarrow {}^4I_{15/2}$). Red emission appears due to the $^4F_{9/2} \rightarrow {}^4I_{15/2}$ de-excitation which could be additionally intensified by the non-radiative $^4F_{7/2} \rightarrow {}^4F_{9/2}$ relaxation. The strengthening of the red emission in YGF-L and Gd-H samples could be a consequence of the appearance of an additional mechanism which involves a successive energy transfer by three photons excitation, as it is corroborated in our previous work [29] and also in [30], but further studies are needed to confirm it. Weak blue emission at 409 nm is due to radiative relaxation of the highest $^2H_{9/2}$ state, which is populated by successive energy transfer [29,31–33]. Since the intensity of each emission is determined by the probability of radiative and non-radiative transitions in particles, as well as their crystallinity, the calculated CIE color coordinates differ, as it is shown in Figure 9c.

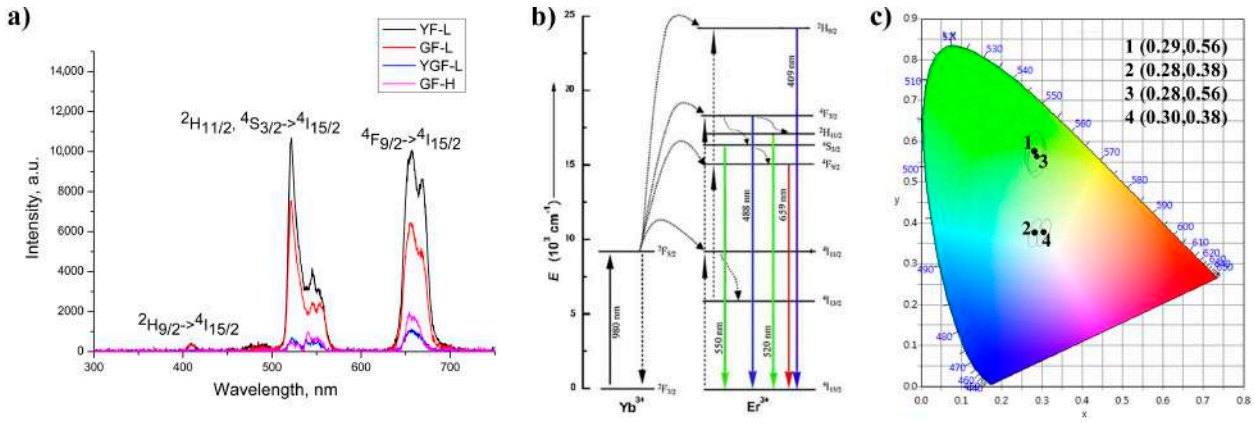

Figure 9. Up-conversion spectrum of the samples excited at 976 nm (**a**), energy level diagram of theYb^{3+}/Er^{3+}couple with radiative transitions marked by solid vertical blue, green and red lines (**b**), CIE diagram in which 1: YF-L; 2: YGF-L; 3: GF-L; and 4: GF-H (**c**).

Evidently, the luminescence of YF-L and GF-L samples is much stronger than that of the YGF-L and GF-H ones. For these samples, temperature sensing capability was determined in the physiologically relevant range of temperatures from 25 °C to 50 °C, using the LIR method. The LIR method for temperature measurement utilizes the intensity ratio of emissions from a pair of closely spaced upper levels, that can be considered as thermally coupled (TCL) [34]. TCL means that these levels have such a small energy difference that the higher level is thermally populated from the lower, so that their relative population follows a Boltzmann distribution. The LIR of spectral lines arising from the transitions from the TCLs level to a common terminal level is [35]:

$$\mathrm{LIR(T)} = \frac{\mathrm{I_H(T)}}{\mathrm{I_L(T)}} = \mathrm{B}\cdot e^{-\frac{\Delta E_{HL}}{k\cdot T}} \quad (2)$$

where $I_{H,L}$ are the luminescence intensities from the upper (H) and lower (L) TCLs to the terminal level radiative transition; ΔE_{HL}—the energy difference between these two levels; k—the Boltzmann constant; and T—the absolute temperature. B is the temperature invariant parameter depending on the host material.

The potential of a material for temperature measurement applications is quantified through the absolute and relative change in the LIR with temperature. The absolute sensitivity of LIR to temperature is given by the partial derivative:

$$S_a = \left|\frac{\partial LIR}{\partial T}\right| = \frac{\Delta E_{HL}}{kT^2}\cdot B\cdot e^{-\frac{\Delta E_{HL}}{k\cdot T}} \quad (3)$$

The relative sensitivity is given by:

$$S_r = \frac{S_a}{LIR} = \frac{\Delta E_{HL}}{kT^2}\cdot 100\% \quad (4)$$

The accuracy and precision of an LIR-based temperature measurement system depend on the sensitivities given above, and also on many characteristics of the measurement system, among which the signal/noise ratio in the captured spectrogram is the most important. However, all characteristics that cause measurement uncertainty can be jointly quantified by the standard deviation of the measured LIRs, obtained over many measurements, taken at a certain fixed temperature. If we denote this quantity by σ_a, the precision of the temperature measurement ΔT can be calculated by the expression:

$$\Delta T = \frac{\sigma_a}{S_a} \quad (5)$$

The accuracy of the measurement is, to the great extent, equal to the precision ΔT defined above, but it also includes additional non-measurable parameters, such as the accuracy of setting the real sample temperature and a possible error due to local heating, which both we considered negligible.

The green parts of spectrograms recorded for YF-L and GF-L in the physiologically interesting temperature range of 25 °C to 50 °C, are shown in Figure 10a,b. A clear decrease in the intensity of individual lines with increasing temperature is clearly notable. The difference in the change rate in the intensity of individual lines is not visible to the naked eye because of the relatively narrow temperature range. In the Yb-Er^{3+} type systems, TCL levels which are of interest are usually $^4S_{3/2}$ and $^2H_{11/2}$ levels of Er^{3+}, and their transitions to the level $^4I_{15/2}$, are taken to calculate the LIR. These transitions are traditionally labeled as 550 nm and 520 nm in Figure 9b, although they have slightly different values, as can be seen in Figure 10. Also, it is evident that there are more than these two lines in the luminescence spectra shown in Figure 10, and that line intensities cannot simply be read as the local maxima of the spectrograms. Therefore, more realistic values of the centers and widths of these lines were obtained by deconvoluting of the recorded spectrograms, using the fitting that assumes a Gaussian shape of the lines. The initial values for the deconvolution process, performed using MATLAB, were determined from the spectrograms as the positions and widths of the obvious peaks. The resulting LIRs for different temperatures are shown in Figure 11a,b.

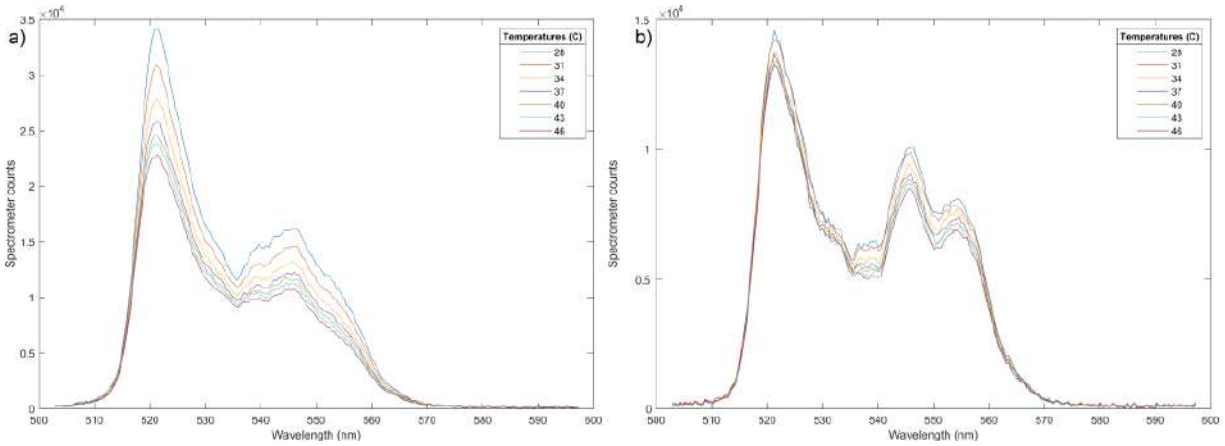

Figure 10. Temperature-dependent UC emission spectra of the YF-L (**a**) and GF-L (**b**) in the wavelength range of 500–600 nm.

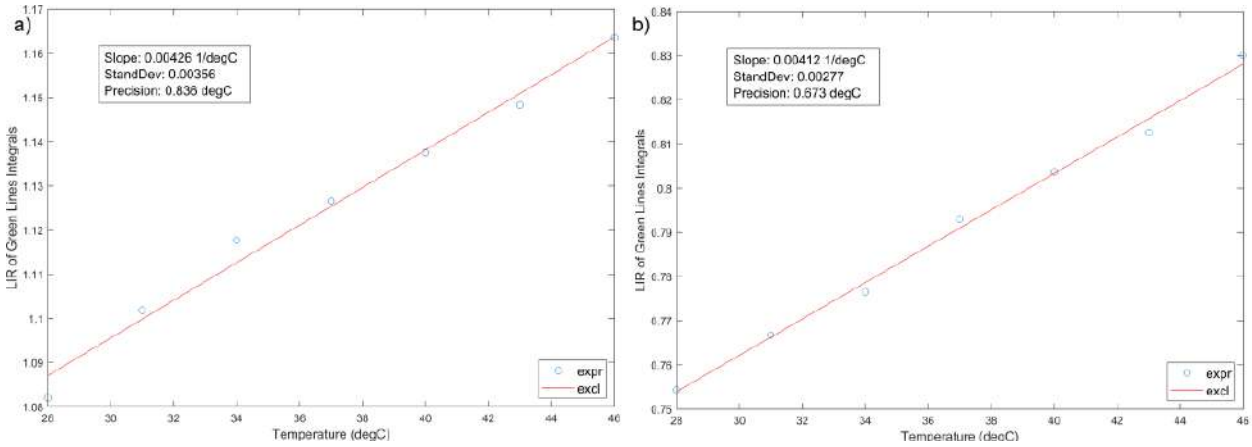

Figure 11. LIR values of YF-L (**a**) and GF-L (**b**) as a function of temperature (dots) and the corresponding line obtained by linear fitting.

The obtained experimental data can be fitted using Equation (2), although in such a narrow temperature range, the linear approximation is quite correct. The slope of both linear curves is equal to Sa = 0.0042 $°C^{-1}$, which can be considered as the absolute sensitivity for temperature measurement in the temperature interval of interest. The relative sensitivity has, according to Equation (4), strong temperature dependance, but it can also be approximated with a constant value in the interval of interest, which is equal to $S_r \approx Sa/LIR_{310}$, where LIR_{310} is the LIR in the middle of the interval, see Figure 11. The relative sensitivities are therefore 0.38%/°C and 0.53%/°C, for YF-L and GF-L samples, respectively. These values are smaller than those obtained using (4) when the energy differences ΔE_{HL} of the levels whose centers are read as local maxima of the spectrogram in Figure 10 are used. This phenomenon is described in [36], while later in [37] is shown that it occurs, to a greater or lesser extent, in most of the investigated materials. It is mainly caused by non-radiative energy transitions, overlapping the TCL spectra, and luminescence originating from other energy levels.

The measurement uncertainty in this work was determined as the standard deviation of LIR measurement, taken separately for both samples on the set of results obtained in 32 consecutive measurements at the temperature of 37 °C. These quantities in principle depend on temperature, but in our measurements, we consider the value obtained at 37 °C as a valid one over the relatively narrow temperature range. The calculated values of the uncertainty for the YF-L and GF-L samples are σ_{YF} = 0.0036 and σ_{GF} = 0.0028, respectively.

The precisions of measurement ΔT_{YF} of 0.84 °C and ΔT_{GF} of 0.67 °C for the YF-L and GF-L samples, respectively, are calculated using Equation (5). These values are slightly higher than those reported in other studies of similar systems [8], which is due to the lower relative sensitivity, discussed in the text above, and the higher noise in the spectrogram originating from the recording method, based on a single laser pulse of 10 ms, without averaging.

To monitor the intracellular uptake and non-specific cell labelling in vitro, GF-L unshelled peanuts-shaped particles were incubated with MRC-5 and A549 cells. Laser scanning microscopy images are shown in Figures 12 and 13. The bright field images of the cells shown in Figures 12a and 13a, reveal that a characteristic fibroblast-like shape was preserved in all cells incubated with GF-L, so they maintained same growth pattern as non-treated control cells. A pseudo color images of the cells auto-fluorescence upon femtosecond excitation at 730 nm are shown in Figures 12b and 13b, whilst the pseudo color images of GF-L mesocrystals upon excitation at 976 nm are given in Figures 12c and 13c. Overlapping the images marked with "b" and "c" in Figures 12 and 13 implies that GF-L mesocrystals (visible as green fluorescence spots) are positioned in the cells cytoplasmic area adjacent to the plasma membrane, in both cell lines. Such positioning, without disturbing cells nuclei confirms successful cell labeling and enables the sensing of the temperature in cells. Laser scanning microscopy images were used further to assess the cell morphology parameters and "occupation degree" of cells by mesocrystals (based on the fluorescence). Obtained results are presented in Figure 14. In both cell types, none of the tested morphological parameters exhibited statistically significant change following the treatment with the GF-L mesocrystals. Cell diameter, surface and nucleus/cytoplasmic ratio remained of the approximately the same values as in non-treated cells. Nucleus circularity index was also unchanged. As regarding fluorescence levels in MRC-5 and A549, normal cells had around 26% lower pixel intensity (fluorescence) per cell as compared to cancer cells. However, despite this statistically noteworthy result, the difference is not compelling enough to provide selectivity towards cancer cells labeling.

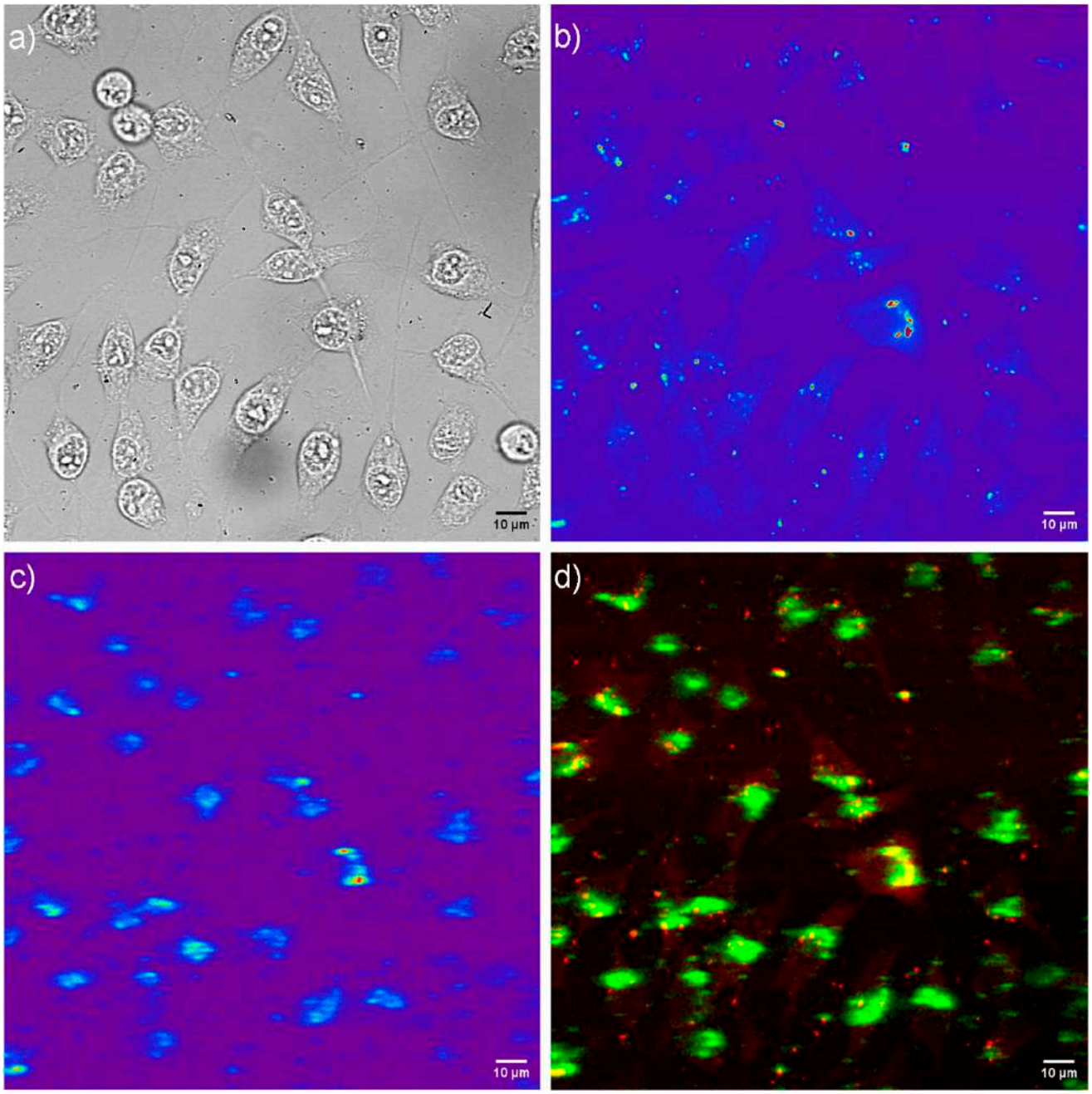

Figure 12. Laser scanning microscopy images of MRC-5 cells incubated with 50 µg mL^{-1} of GF-L mesocrystals; bright field image of cells (**a**), cells auto-fluorescence upon femto-second excitation at 730 nm (**b**), image of GF-L mesocrystals upon continuous wave excitation at 976 nm (**c**), and their positioning in cells, revealed through co-localization of the cell auto-fluorescence and the GF-L photoluminescence (**d**).

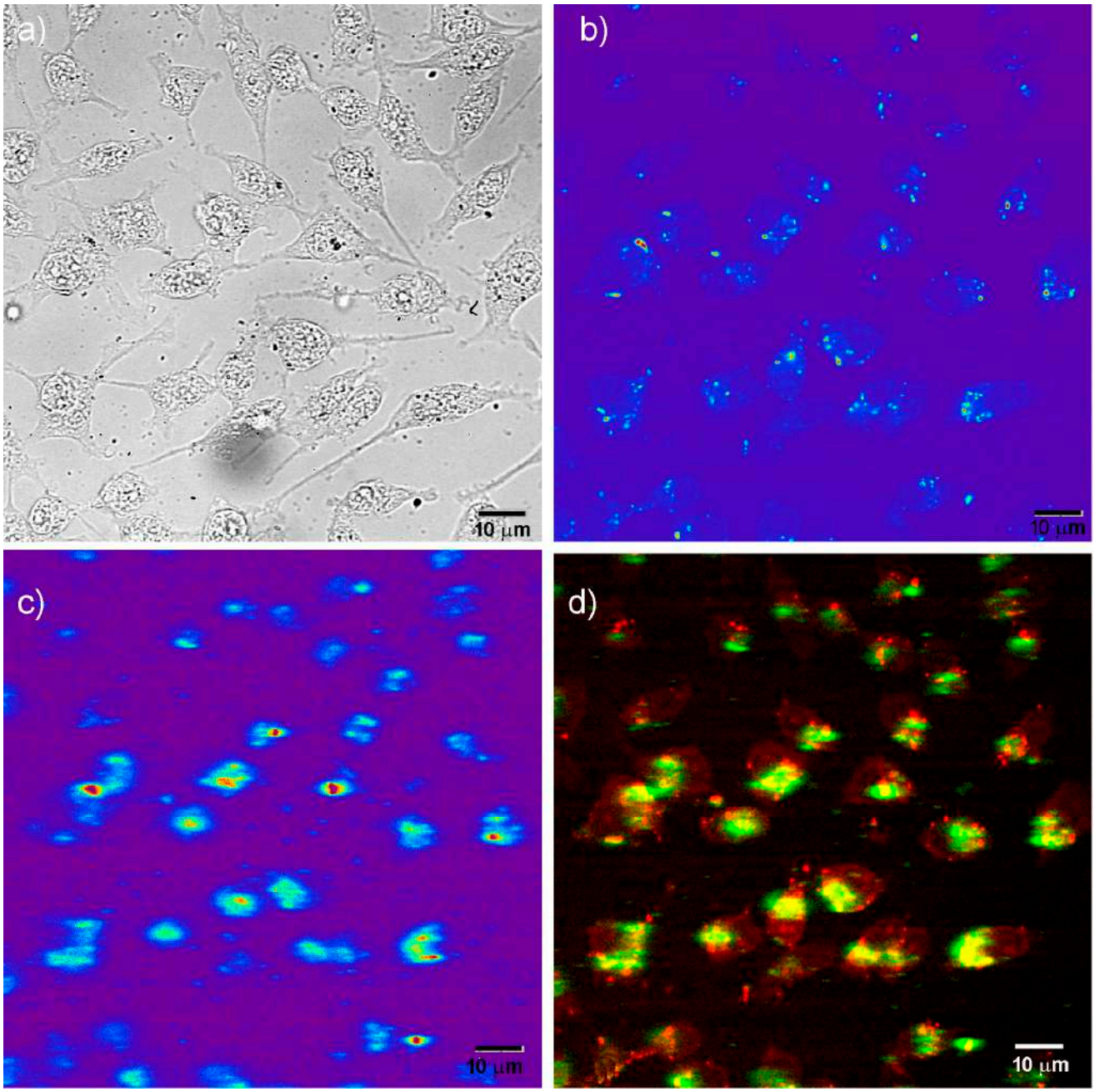

Figure 13. Laser scanning microscopy images of A549 cells incubated with 50 μg mL^{-1} of GF-L mesocrystals; bright field image of cells (**a**), cells auto-fluorescence upon femto-second excitation at 730 nm (**b**), image of GF-L mesocrystals upon continuous wave excitation at 976 nm (**c**), and their positioning in cells, revealed through co-localization of the cell auto-fluorescence and the GF-L photoluminescence (**d**).

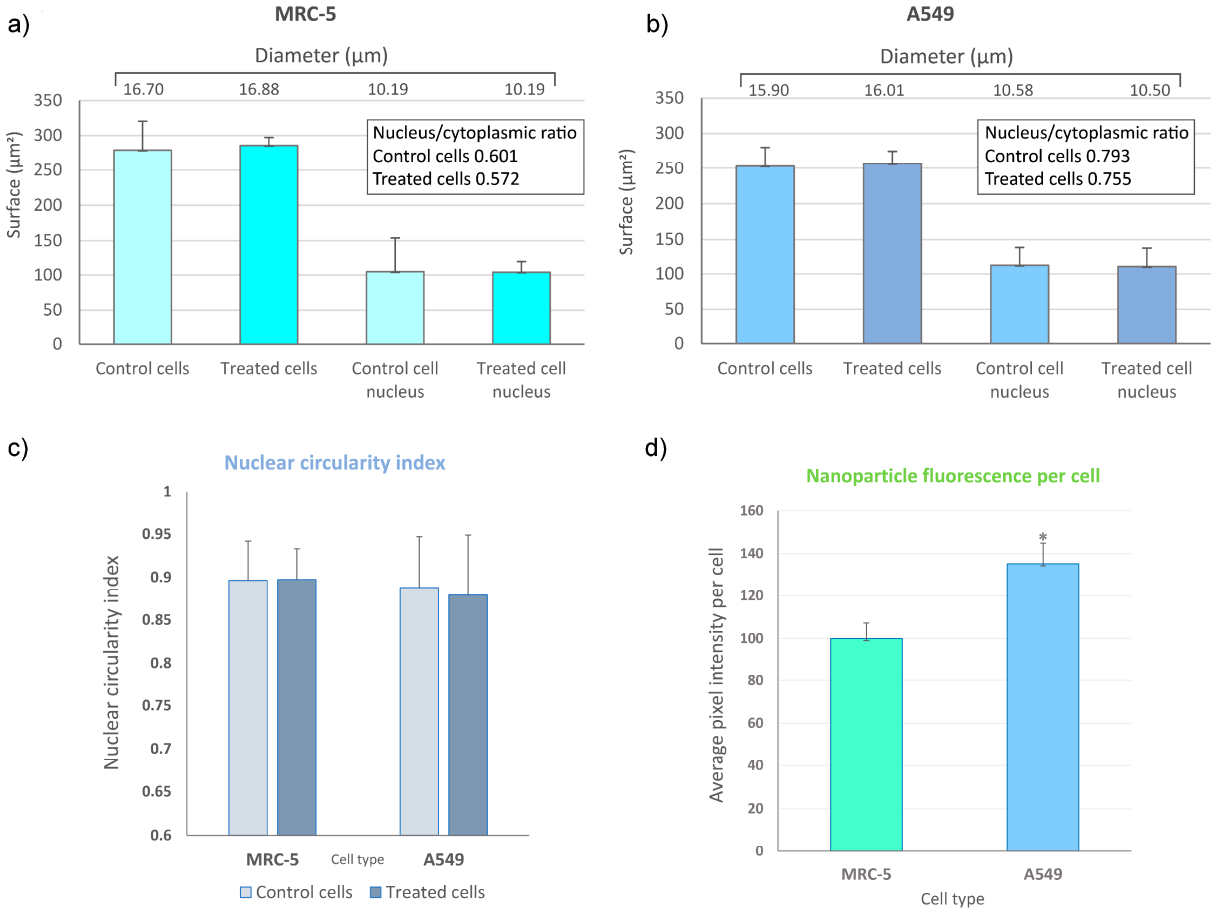

Figure 14. Comparison of cell morphology parameters in terms of average surface, diameter and (in inserts) nucleus/cytoplasmic ratio in control and GF-L-treated group of MRC-5 (**a**) and A549 cells (**b**); nuclear circularity indexes of control and treated cells (**c**); average fluorescence per cell, as calculated from the pixel intensity in filtered images. Measurements were performed by using laser microscopy images and ImageJ software. Statistical significance threshold was $p < 0.05$ and is represented by *(**d**).

4. Discussion

According to the phase diagram of NaF-YF_3 and YF_3-GdF_3 systems [38], the crystallization of the following fluorides could be achieved in function of temperature, $NaYF_4$ in two forms (cubic α phase, *Fm-3m*; and hexagonal β phase, *P63/m*), and three crystal structures of the $Y_{1-x}Gd_xF_3$ phases (orthorhombic β phase, *Pnma*; hexagonal, *P63cm*; and trigonal, *P-3c1* phase). Contrary to our previous work, where we obtained the β-$NaYF_4$:Yb,Er phase under identical processing conditions [39], since the YF_3 and GdF_3 phases show complete miscibility, all samples synthesized in this study, independent of stoichiometry, have the same orthorhombic crystal structure. The XRPD analysis revealed a change in the unit cell parameters due to the substitution of ytterbium by gadolinium and the coexistence of two different particle populations in all samples, which is associated with the formation of monocrystals.

Considerable progress has so far been made in the synthesis of YF_3 particles with different morphologies, such as truncated octahedral-, quadrilateral-, hexagonal-, spherical-, octahedral-, and bundle-like nanocrystals [40]. We also reported the change in the morphology of the YF_3 monocrystal during EDTA-assisted hydrothermal synthesis—provoked by the modification of the processing parameters [29], as well as the compositional change which occurred in the course of sonication [41]. In this study, the change in the particle morphology was detected with the rise of the Gd concentration. In the GF-L sample, a decreased size of particles (compared to the YF-L and YGF-L samples) could be associated

with the higher charge density on their crystal surface, which slows the diffusion of negatively charged fluoride ions leading to a reduction in the crystal growth rate [42]. With the rise of the gadolinium precursor concentration, a change in the morphology is detected. A high tendency towards self-organization of elongated $Gd_{0.8}F_3$:$Yb_{0.18}Er_{0.02}$ monocrystals into two-dimensional rhomboidal layers is probably due to the anchoring of branched chitosan ligands, which are present in a higher content in the GF-H sample.

The existence of chitosan ligands at the particle surface ensures that mesocrystals have a low cytotoxicity. A low cytotoxicity of chitosan-capped YF_3:Yb,Er nanoparticles toward human breast cancer MCF-7 cells and GdF_3:Yb^{3+}/Er^{3+}/Li^+ hollow spheres, reported in the literature [43,44], is in agreement with the results obtained in this study. The viability of both, MRC-5 and A549 cells was highly preserved after a 24-h exposure, being above 80% for all examined concentrations of YF-L and GF-L particles. As demonstrated in our previous study [17], the presence of chitosan amino functional groups at the $\alpha NaYF_4$:Yb,Er UCNPs surface enhances their use for in vitro cell labelling. The same feature is confirmed here for GF-L unshelled peanuts-shaped particles. Their successful incubation in the cytoplasmic region of MRC-5 and A549 cells enables the visualization of cells, and also creates condition for in situ measuring of cell temperature. Morphological parameters of the cell, and especially nucleus, are considered to be indicators of the change in cellular physiological condition. As it is shown here, GF-L mesocrystals did not induce significant change in cell size parameters, excluding large-scale processes such as early-stage necrosis (necrotic volume increase) [45]. Homeostasis of nucleus/cytoplasmic ratio, indicative for many cellular physiologic activities, changes in growth and also pathological processes, was also unchanged [46]. Furthermore, the nucleus circularity index showed that there was also no change in the nucleus morphology. Nuclear circularity index values close to 1 indicate a normal, circular nucleus [25]. All of these parameters in the range of normal cell values did not exclude possibility of mesocrystals affecting the structures and physiology of the cells, but they did show that no morphology- and physiology-changing effects took place. This, together with the results from viability testing using MTT, is overall a good indication of biocompatibility of tested samples at this stage of research. This is of crucial importance, because mesocrystals obtained in this study have potential for application in temperature sensing in the physiologically relevant range of temperatures.

The absolute sensitivity of 0.0042 $°C^{-1}$, and the accuracy of 0.84 °C (YF-L) and 0.67 °C (GF-L) is somewhat lower than the previously published ones related to strongly agglomerated and irregularly shaped $Y_{0.78}Yb_{0.2}Er_{0.02}F_3$ particles obtained through solid-state reactions [19] and from glass ceramics embedded with YF_3:Yb,Tm,Er nanocrystals synthesized using a melt-quenching method [20]. Both were determined for the much wider temperature range, in which the population of Er^{3+} $^2H_{11/2}$ and $^4S_{3/2}$ thermally coupled levels is governed by the Boltzmann distribution, and is not comparable with the thermal sensitivity of the GF_3:Yb,Er phase due to the absence of published data.

5. Conclusions

Biocompatible $Y_{0.8-x}Gd_xF_3$:Yb/Er mesocrystals with an unshelled peanuts-like, and rhombic-layered structure were obtained using chitosan-assisted solvothermal processing. These structures are built from much smaller monocrystals, whose tendency towards self-organization is governed by the quantity of preserved chitosan ligands at their surface. The difference in charge density inside the crystals, induced by the increase in the gadolinium content in the YF_3 host matrix, resulted in a minor change in local symmetry of dopant ions, due to which the shape and intensity of Er^{3+} emission lines varied. The change in the visible green emission intensity with temperature, originating from the thermalization of the $^2H_{11/2}$ and $^4S_{3/2\text{-}4}$ levels of Er^{3+}, is used for testing their capacity for temperature sensing. The detected absolute sensitivity of 0.0042 $°C^{-1}$, the accuracies of 0.84 °C ($Y_{0.8}Yb_{0.18}Er_{0.02}F_3$) and 0.67 °C ($Gd_{0.8}Yb_{0.18}Er_{0.02}F_3$), in vitro cell labeling capacity, and the low cytotoxicity to both, MRC-5 and A549 cells, make them suitable for further optimization towards more specific application in biomedicine.

Author Contributions: Conceptualization, L.M. and I.D.; methodology, I.D. and M.T.; software, L.M., M.E.R., N.T. and M.T.; validation, L.M. and M.E.R.; formal analysis, I.D., M.V., M.M., M.B.; investigation, M.V., M.M., M.B. and N.T.; resources, L.M. and N.I.; data curation, I.D. and M.T.; writing—original draft preparation, I.D. and M.V.; writing—review and editing, L.M. and N.I.; visualization, I.D., M.B. and N.T.; supervision, L.M. and M.T. All authors have read and agreed to the published version of the manuscript.

Funding: The research was funded by the Ministry of Science, Technological Development and Innovation of the Republic of Serbia on the research programs: Grant No. 451-03-47/2023–01/200175 (Institute of Technical Sciences of SASA), Grant No. 451-03-47/2023–01/200288 (Innovative Centre, Faculty of Chemistry, UB) and Grant No. 451-03-47/2023–01/200017 (Vinca Institute of Nuclear Sciences). The M.B. acknowledges funding provided by the Institute of Physics Belgrade, through the grant by Ministry of Science, Technological Development and Innovation of the Republic of Serbia. The full waiver of APC is applied.

Data Availability Statement: Data are contained within the article.

Conflicts of Interest: The authors declare no conflict of interest.

References

1. Auzel, F. Upconversion and Anti-Stokes Processes with f and d Ions in Solids. *Chem. Rev.* **2004**, *104*, 139–173. [CrossRef] [PubMed]
2. Haase, M.; Schäfer, H. Upconverting nanoparticles. *Angew. Chem. Int. Ed.* **2011**, *50*, 5808–5829. [CrossRef] [PubMed]
3. Liang, G.; Wang, H.; Shi, H.; Wang, H.; Zhu, M.; Jing, A.; Li, J.; Li, G. Recent progress in the development of upconversion nanomaterials in bioimaging and disease treatment. *J. Nanobiotechnol.* **2020**, *18*, 154. [CrossRef] [PubMed]
4. Li, Y.; Liu, C.; Zhang, P.; Huang, J.; Ning, H.; Xiao, P.; Hou, Y.; Jing, L.; Gao, M. Doping Lanthanide Nanocrystals With Non-lanthanide Ions to Simultaneously Enhance Up- and Down-Conversion Luminescence. *Front. Chem.* **2020**, *8*, 832. [CrossRef] [PubMed]
5. Xie, J.; Hu, W.; Tian, D.; Wei, Y.; Zheng, G.; Huang, L.; Liang, E. Selective growth and upconversion photoluminescence of Y-based fluorides: From $NaYF_4$: Yb/Er to YF_3: Yb/Er crystals. *Nanotechnology* **2020**, *31*, 505605. [CrossRef] [PubMed]
6. Ghazy, A.; Safdar, M.; Lastusaari, M.; Savin, H.; Karppinen, M. Advances in upconversion enhanced solar cell performance. *Sol. Energy Mater. Sol. Cells* **2021**, *230*, 111234. [CrossRef]
7. Yanykin, D.V.; Paskhin, M.O.; Simakin, A.V.; Burmistrov, D.E.; Pobedonostsev, R.V.; Vyatchinov, A.A.; Vedunova, M.V.; Kuznetsov, S.V.; Ermakova, J.A.; Alexandrov, A.A.; et al. Plant Photo-chemistry under Glass Coated with Upconversion Luminescent Film. *Appl. Sci.* **2022**, *12*, 7480. [CrossRef]
8. Qiu, X.; Zhou, Q.; Zhu, X.; Wu, Z.; Feng, W.; Li, F. Ratiometric upconversion nanothermometry with dual emission at the same wavelength decoded via a time-resolved technique. *Nat. Commun.* **2020**, *11*, 4. [CrossRef]
9. Chen, D.; Wan, Z.; Zhou, Y.; Huang, P.; Zhong, J.; Ding, M.; Xiang, W.; Liang, X.; Ji, Z. Bulk glass ceramics containing Yb3+/Er3+: β-$NaGdF_4$ nanocrystals: Phase-separation-controlled crystallization, optical spectroscopy and upconverted temperature sensing behavior. *J. Alloys Compd.* **2015**, *638*, 21–28. [CrossRef]
10. Xi, J.; Ding, M.; Zhang, M.; Zhang, H.; Chen, D.; Ji, Z. Monodispersed YF_3: $Ce^{3+}/Tb^{3+}/Eu^{3+}$ mesocrystals: Hydrothermal synthesis and optical temperature sensing behavior. *J. Mater. Sci. Mater Electron.* **2017**, *28*, 9489–9494. [CrossRef]
11. Lojpur, V.; Nikolic, M.; Dramicanin, M.D. Luminescence thermometry below room temperature via up-conversion emission of Y_2O_3:Yb^{3+},Er^{3+} nanophosphors. *J. Appl. Phys.* **2014**, *115*, 203106. [CrossRef]
12. Hao, H.; Lu, Z.; Lu, H.; Ao, G.; Song, Y.; Wang, Y.; Zhang, X. Yb^{3+} concentration on emission color, thermal sensing and optical heater behavior of Er^{3+} doped $Y_6O_5F_8$ phosphor. *Ceram. Int.* **2017**, *43*, 10948–10954. [CrossRef]
13. Li, L.; Wang, W.; Chen, H.; Li, S.; Zhang, Q.; Pan, Y.; Li, Y. Optical thermometry based on upconversion luminescence of $Ba_3Gd_2F_{12}$: Yb^{3+}/Er^{3+} nanocrystals embedded in glass ceramics. *J. Non-Cryst. Solids* **2021**, *573*, 121142. [CrossRef]
14. Bao, R.; Yu, L.; Ye, L.; Zhang, X.; Wang, L.G. Compact and sensitive Er^{3+}/Yb^{3+}co-doped YAG single crystal optical fiber thermometry based on up-conversion luminescence. *Sens. Actuators A* **2018**, *269*, 182–187. [CrossRef]
15. Muhr, V.; Wilhelm, S.; Hirsch, T.; Wolfbeis, O. Upconversion Nanoparticles: From Hydrophobic to Hydrophilic Surfaces. *Acc. Chem. Res.* **2014**, *47*, 3481–3493. [CrossRef]
16. Wang, L.Y.; Zhang, Y.; Zhu, Y.Y. One-Pot Synthesis and Strong Near-Infrared Upconversion Luminescence of Poly(acrylic acid)-Functionalized YF_3:Yb^{3+}/Er^{3+} Nanocrystals. *Nano Res.* **2010**, *3*, 315–325. [CrossRef]
17. Mancic, L.; Djukic-Vukovic, A.; Dinic, I.; Nikolic, M.; Rabasovic, M.; Krmpot, A.; Costa, A.; Marinkovic, B.; Mojovic, L.; Milosevic, O. One-step synthesis of amino-functionalized upconverting $NaYF_4$:Yb,Er nanoparticles for in vitro cell imaging. *RSC Adv.* **2018**, *8*, 27429–27437. [CrossRef]
18. Mancic, L.; Djukic-Vukovic, A.; Dinic, I.; Nikolic, M.; Rabasovic, M.; Krmpot, A.; Costa, A.; Trisic, D.; Lazarevic, M.; Mojovic, L.; et al. NIR photo-driven upconversion in NaYF4:Yb,Er/PLGA particles for in vitro bioimaging of cancer cells. *Mater. Sci. Eng. C* **2018**, *91*, 597–605. [CrossRef]

19. Ciric, A.; Aleksic, J.; Barudžija, T.; Antic, Ž.; Đorđevic, V.; Medic, M.; Periša, J.; Zekovic, I.; Mitric, M.; Dramicanin, M. Comparison of Three Ratiometric Temperature Readings from the Er^{3+} Upconversion Emission. *Nanomaterials* **2020**, *10*, 627. [CrossRef]
20. Chen, D.; Liu, S.; Li, X.; Yuan, S.; Huan, P. Upconverting luminescence based dual-modal temperature sensing for $Yb^{3+}/Er^{3+}/Tm^{3+}$: YF_3 nanocrystals embedded glass ceramic. *J. Eur. Ceram. Soc.* **2017**, *37*, 4939–4945. [CrossRef]
21. Bakhmetyev, V.V.; Dorokhina, A.M.; Keskinova, M.V.; Mjakin, S.V.; Vlasenko, A.B.; Lebedev, L.A.; Malygin, V.V.; Sychov, M.M. Synthesis and characterization of finely dispersed phosphors doped with rare-earth metal ions for enhanced photodynamic therapy of cancer. *Chem. Pap.* **2019**, *74*, 787–797. [CrossRef]
22. Yin, W.; Zhao, L.; Zhou, L.; Gu, Z.; Liu, X.; Gan Tian, G.; Jin, S.; Yan, L.; Ren, W.; Xing, G.; et al. Enhanced Red Emission from GdF_3:Yb^{3+},Er^{3+} Upconversion Nanocrystals by Li+ Doping and Their Application for Bioimaging. *Chem. Eur. J.* **2012**, *18*, 9239–9245. [CrossRef] [PubMed]
23. TOPAS. *General Profile and Structure Analysis Software for Powder Diffraction Data, V4.2*; Bruker AXS GmbH: Karlsruhe, Germany, 2009.
24. *ISO 10993-5:2009(E)*; Biological evaluation of medical Devices. Part 5: Tests for In Vitro Cytotoxicity. International Organization for Standardization [ISO]: Geneva, Switzerland, 2009.
25. Ankam, S.; Teo, K.K.B.; Pohan, G.; Ho, W.L.S.; Lim, K.C.; Yim, K.F.E. Temporal Changes in Nucleus Morphology, Lamin A/C and Histone Methylation During Nanotopography-Induced Neuronal Differentiation of Stem Cells. *Front. Bioeng. Biotechnol.* **2018**, *6*, 69. [CrossRef] [PubMed]
26. Latif, I.A.; Abdullah, H.M.; Saleem, H.M. Electrical and Swelling Study of Different Prepared Hydrogel. *Am. J. Polym. Sci.* **2016**, *6*, 50–57.
27. Silva, S.M.L.; Braga, C.R.C.; Fook, M.V.L.; Raposo, C.M.O.; Carvalho, L.H.; Eduardo, L.; Canedo, E.L. Application of infrared spectroscopy to analysis of chitosan/clay nanocomposites. In *Infrared Spectroscopy—Materials Science, Engineering and Technology*; Theophanides, T., Ed.; InTech: London, UK, 2012; ISBN 978-953-51-0537-4.
28. Yang, Y.; Cui, J.; Zheng, M.; Hu, C.; Tan, S.; Xiao, Y.; Yang, Q.; Liu, Y. One-step synthesis of amino-functionalized fluorescent carbon nanoparticles by hydrothermal carbonization of chitosan. *Chem. Commun.* **2012**, *48*, 380–382. [CrossRef]
29. Dinic, I.Z.; Mancic, L.T.; Rabanal, M.E.; Yamamoto, K.; O'Hara, S.; Tamura, S.; Koji, T.; Costa, A.M.L.M.; Marinkovic, B.A.; Milosevic, O.B. Compositional and structural dependence of up-converting rare earth fluorides obtained through EDTA assisted hydro/solvothermal synthesis. *Adv. Powder Technol.* **2017**, *28*, 73–82. [CrossRef]
30. Low, N.M.P.; Major, A.L. Effects of preparation on the anti-Stokes luminescence of Er -activated rare-earth phosphors. *J. Lumin.* **1974**, *4*, 357. [CrossRef]
31. Li, C.; Lin, J. Rare earth fluoride nano-/microcrystals: Synthesis, surface modification and application. *J. Mater. Chem.* **2010**, *20*, 6831–6847. [CrossRef]
32. Vetrone, F.; Naccache, R.; Juarranz de la Fuente, A.; Sanz-Rodríguez, F.; Blazquez-Castro, A.; Martin Rodriguez, E.; Jaque, D.; Garcia Sole, J.; Capobianco, J.A. Intracellular imaging of HeLa cells by non-functionalized $NaYF_4$:Er^{3+},Yb^{3+} upconverting nanoparticles. *Nanoscale* **2010**, *2*, 495–498. [CrossRef]
33. Vetrone, I.F.; Boyer, J.C.; Capobianco, J.A.; Speghini, A.; Bettinelli, M.J. Significance of Yb^{3+} concentration on the upconversion mechanisms in co-doped Y_2O_3:Er^{3+},Yb^{3+} nanocrystals. *J. App. Phys.* **2004**, *96*, 661–667. [CrossRef]
34. Wade, S.A.; Collins, S.F.; Baxter, G.W. Fluorescence intensity ratio technique for optical fiber point temperature sensing. *J. Appl. Phys.* **2003**, *94*, 4743. [CrossRef]
35. Ćirić, A.; Gavrilović, T.; Dramićanin, M.D. Luminescence Intensity Ratio Thermometry with Er3+: Performance Overview. *Crystals* **2021**, *11*, 189. [CrossRef]
36. Wade, S.A. Temperature Measurement Using Rare Earth Doped Fibre Fluorescence. Ph.D. Thesis, Victoria University, Melbourne, Australia, 1999.
37. Wang, X.; Liu, Q.; Bu, Y.; Liu, C.-S.; Liu, T.; Yan, X. Optical temperature sensing of rare-earth ion doped phosphors. *RSC Adv.* **2015**, *5*, 86219–86236. [CrossRef]
38. Yasyrkina, D.S.; Kuznetsov, S.V.; Ryabova, A.V.; Pominova, D.V.; Voronov, V.V.; Ermakov, R.P.; Fedorov, P.P. Dependence of quantum yields of up-conversion luminescence on the composition of fluorite type solid solution $NaY_{1\_x\_y}Yb_xEr_yF_4$. *Nanosyst. Phys. Chem. Math.* **2013**, *5*, 648–656.
39. Vukovic, M.; Mancic, L.; Dinic, I.; Vulic, P.; Nikolic, M.; Tan, Z.; Milosevic, O. The gadolinium effect on crystallization behavior and luminescence of β-$NaYF_4$:Yb,Er phase. *Int. J. Appl. Ceram. Technol.* **2020**, *17*, 1445–1452. [CrossRef]
40. Qian, L.; Zai, J.; Chen, Z.; Zhu, J.; Yuan, Y.; Qian, X. Control of the morphology and composition of yttrium fluoride via a salt-assisted hydrothermal method. *CrystEngComm* **2010**, *12*, 199–206. [CrossRef]
41. Vukovic, M.; Dinic, I.; Jardim, P.; Markovic, S.; Veselinovic, L.; Nikolic, M.; Mancic, L. The low-temperature sonochemical synthesis of up-converting β $NaYF_4$: Yb,Er mesocrystals. *Adv. Powder Technol.* **2022**, *33*, 103403. [CrossRef]
42. Vidyakina, A.A.; Kolesnikov, I.E.; Bogachev, N.A.; Skripkin, M.Y.; Tumkin, I.I.; Lähderanta, E.; Mereshchenko, A.S. Gd^{3+}-Doping Effect on Upconversion Emission of $NaYF_4$: Yb^{3+}, Er^{3+}/Tm^{3+} Microparticles. *Materials* **2020**, *13*, 3397. [CrossRef]
43. Gayathri, S.; Ghosh, O.S.N.; Viswanath, A.K.; Sudhakara, P.; Reddy, M.J.K.; Shanmugharaj, A.M. Synthesis of YF_3: Yb, Er upconverting nanofluorophores using chitosan and their cytotoxicity in MCF-7 cells. *Int. J. Biol. Macromol.* **2015**, *72*, 1308–1312. [CrossRef]

44. Lv, R.; Gai, S.; Dai, Y.; Niu, N.; He, F.; Yang, P. Highly Uniform Hollow GdF_3 Spheres: Controllable Synthesis, Tuned Luminescence, and Drug-Release Properties. *ACS Appl. Mater. Interfaces* **2013**, *5*, 10806–10818. [CrossRef]
45. Barros, L.F.; Hermosilla, T.; Castro, J. Necrotic volume increase and the early physiology of necrosis. *Comp. Biochem. Physiol. A* **2001**, *130*, 401–409. [CrossRef] [PubMed]
46. Balachandra, S.; Sarkar, S.; Amodeo, A.A. The Nuclear-to-Cytoplasmic Ratio: Coupling DNA Content to Cell Size, Cell Cycle, and Biosynthetic Capacity. *Annu. Rev. Genet.* **2022**, *56*, 165–185. [CrossRef] [PubMed]

Disclaimer/Publisher's Note: The statements, opinions and data contained in all publications are solely those of the individual author(s) and contributor(s) and not of MDPI and/or the editor(s). MDPI and/or the editor(s) disclaim responsibility for any injury to people or property resulting from any ideas, methods, instructions or products referred to in the content.

Slight cooling during growth induced changes in filamentous fungi hypha mitochondrial morphology

Aleksandra Vitkovac[1], Tanja Pajić[1*], Marta Bukumira[2], Marina Stanić[3], Mihailo Rabasović[2], Nataša Todorović[4]

[1] University of Belgrade, Faculty of Biology, Department for General Physiology and Biophysics, Belgrade, Serbia (Studentski trg 16, 11158); e-mail: b1039_2022@stud.bio.bg.ac.rs, tpajic@bio.bg.ac.rs
[2] University of Belgrade, Institute of Physics, Laboratory for Biophysics, Belgrade, Serbia (Pregrevica 118, 11080); e-mail: marta@ipb.ac.rs , rabasovic@ipb.ac.rs
[3] University of Belgrade, Institute for Multidisciplinary Research, Department of Life Sciences, Belgrade, Serbia (Bulevar despota Stefana 142, 11060); e-mail: mstanic@imsi.rs
[4] University of Belgrade, Institute for Biological Research "Siniša Stanković", Department of Neurophysiology, Belgrade, Serbia (Bulevar despota Stefana 142, 11060); e-mail: nara@ibiss.bg.ac.rs
* *Corresponding author*

DOI: 10.46793/ICCBI23.334V

Abstract: Adaptive changes in mitochondrial morphology are associated with changes in the mitochondrial function and metabolic fitness of eukaryotic cells. We previously described in young hyphae of the filamentous fungus *Phycomyces blakesleeanus* a dramatic effect of an increase in ambient temperature during growth: a 3°C warmer environment compared with a control temperature of 22°C resulted in the appearance of long elongated ("tubular") mitochondria accompanied by an increase in lipid droplet density. Here, we examined how cooler ambient temperature (18°C) during growth affects mitochondrial morphology in *P. blakesleeanus* compared with the control grown at 22°C. We used two-photon fluorescence imaging (TPEF) of live hyphae stained with the vital mitochondrial dye rhodamine 123. Extraction of relevant parameters (number, size, and shape of mitochondria) from TPEF images was performed using the Ilastik machine learning-based software. The suitability of the Ilastik analysis was compared with the Particle Analysis (ImageJ). Cold treatment resulted in the appearance of tubular mitochondrial morphology that was absent in the control group. Tubular mitochondrial morphology appears to be an adaptive feature that occurs in both warmer and colder conditions and is likely part of the stress response.

Keywords: *Phycomyces*, Imaging, TPEF, Machine-learning, Ilastik

1. Introduction

Mitochondria are very plastic organelles capable of morphologically adapting in order to meet cellular needs. The conditions that require more efficient quality control or greater respiratory capacity lead to fragmentation or fusion of mitochondria,

respectively [1]. We have previously shown that a 3°C warmer environment induces the appearance of tubular mitochondria in the filamentous fungus *Phycomyces blakesleeanus* [2]. Here we investigate the effects of a 3°C cooler environment on mitochondrial morphology.

2. Methods

Hyphal cells of the unicellular filamentous fungus *Phycomyces blakesleeanus* (Burgeff), wt (NRRL 1555(−)), were grown in illuminated stationary plates at 22°C for 16-21 h, as described previously [3], or at 18°C for cold treatment. Mitochondria stained with 5 μM rhodamine123 (Rhd123) were imaged *in vivo* by two-photon fluorescence microscopy (TPEF) of hyphae. Images were obtained from five separate cultures. For two-photon excitation of Rhd123, we used a Ti:Sa laser tuned to 800 nm (160 fs pulse duration, 76 MHz repetition rate) focused with the Zeiss Plan Neofluar 40x1.3 objective. The signal was detected through a MF530/43 bandpass interference filter (ThorLabs, USA). Details of the experimental setup for TPEF were described in [4]. Raw images were analyzed in both Ilastik and ImageJ Particle Analysis software packages using individually thresholded images to achieve high-quality segmentation of the bright structures representing mitochondria. Only images with a sufficiently high signal-to-noise ratio (to clearly distinguish the structures from the background) were analyzed. Statistics: ANOVA with multiple comparisons and Holm-Sidac correction, and an unpaired two-tailed t test with Welch's correction for unequal variances. Confidence levels for statistical significance were: 0.05 (*), 0.01 (**), 0.005 (***).

3. Results and Discussion

TPEF images showed that Rhd123-stained mitochondria of different shapes and sizes were distributed throughout the control hyphae (n = 6) and that there was no conspicuous region of high density in the growing hyphal tip (Fig. 1a, left). In cold-treated hyphae (n = 12), there was a similar range of mitochondrial shapes and sizes as in the control group, except for some longer mitochondria (Fig. 1a, right). To quantify mitochondrial morphology in an efficient and accurate manner, we trained a machine learning-based software routine in Ilastik to sort them into groups: round, ellipsoid, and elongated. The classifications obtained, such as the example shown in Fig. 1b (a colored mask superimposed on the image), matched well with the initial images. The same images were subjected to ImageJ Particle Analysis (Fig. 1c), and the obtained morphological measures were compared with the Ilastik-derived data for each hypha (Fig. 1d,e). The number of mitochondria determined by ImageJ was significantly lower than the number counted by Ilastik ($p < 0.0001$) (Fig. 1d left), while the total area occupied by mitochondria was similar in ImageJ and Ilastik ($p=0.46$) (Fig. 1d right). Visual inspection of the ImageJ-generated masks confirmed that many individual mitochondria were not well separated. Therefore, we analyzed the Ilastik -generated dataset in more detail. The results are shown in Fig. 2.

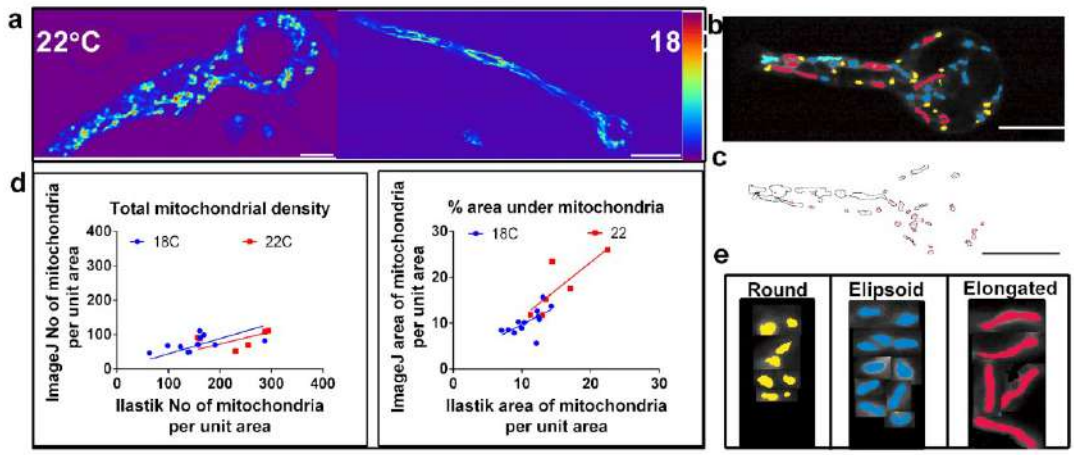

Figure 1. Mitochondrial morphology analysis from *P. blakesleeanus* hypha TPEF images. a.) Representative TPEF images of Rhd123-stained hypha grown in control (22°C) and cool (18°C) conditions. The color bar on the right, blue indicates lowest signal values. b-c.) Results of segmentation during image analysis using Ilastik (b) and Particle Analysis in ImageJ (c). d.) Comparison of values obtained by Ilastik and ImageJ analysis: Mitochondrial density (left) and percent of hyphal area occupied by mitochondria (right). All points are shown, with obtained linear fit coefficients: for mitochondrial density, k = 0.44 ± 0.04 (18°C) and k = 0.36 ± 0.05 (22°C); for % area under mitochondria, k = 0.76 ± 0.3 (18°C) and k=1.2±0.4 (22°C). e.) Representative examples of shapes of mitochondria for each of the main morphology groups: round, ellipsoid and elongated. Scales are shown in the bottom of images: a.)10 μm (left) and 20 μm (right); b.) 10 μm; c.) 10 μm.

We found that the number of mitochondria per unit area of hyphae (Fig. 2a) was lower in the 18°C group, which is consistent with the expected changes in mitochondrial morphology toward greater connectivity during adaptation to stress. On the other hand, the finding that the total area under the mitochondria (Fig. 2b) decreased with cooling suggests an increase in mitophagy, or alternatively, that increased fragmentation of mitochondria resulted in a portion of very small structures below the detection limit (submicron size). Overall, these results suggest that the dynamic restructuring of the mitochondrial network occurs in cooled hyphae. We examined a subset of representative hyphae from both groups in more detail. The density of each morphological type was similar in both groups, so the data were pooled (Fig. 2c). The length of the mitochondria in each morphological group is shown in Fig. 2d for the 22°C group and in Fig. 2e for the 18°C group. Significantly longer elongated (tubular) mitochondria were found in the 18°C group compared with the 22°C group (Fig. 2f).

3. Conclusions

The tubular morphology of mitochondria is an adaptive feature that occurs under colder conditions, similar to the changes previously observed in warmer environments, and is likely part of the stress response. Slight changes in ambient temperature can elicit a mitochondrial response, that is, dynamic changes in morphology.

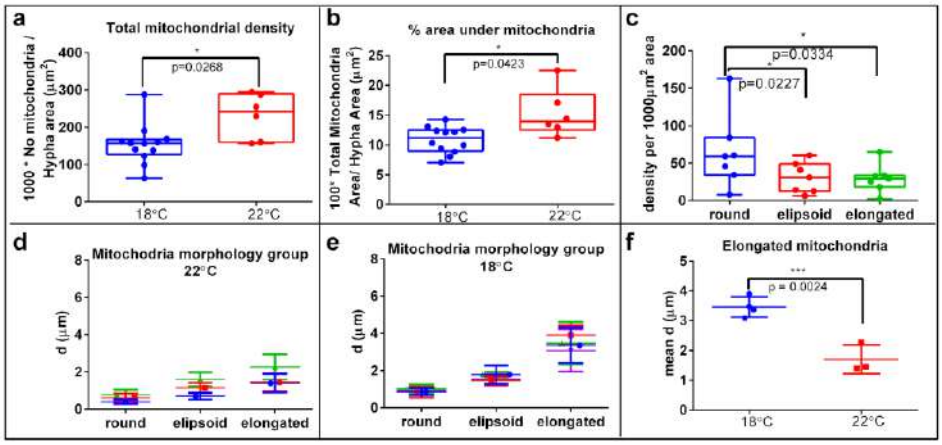

Figure 2. Parameters of mitochondrial morphology obtained from Ilastik image analysis, shown as box and whiskers plots enclosing the 25th and 75th percentile range with the line representing the median and the whiskers extending to the minimal and maximal value, all points shown. (a.,b.,f.) Comparison of hypha grown at 18°C (n=12) and at 22°C (n=6). T-test with Welch's correction: a.) Mitochondrial density (defined as the number of mitochondria per 1000 µm² of hypha area). b.) Mitochondrial area in a hypha normalized to the area of that hypha (% area under mitochondria). c.) The density of mitochondria belonging to each morphological type (round, ellipsoid, elongated) from pooled subsets of Control (n =3) and Cold-treated (n=4) hypha images. Anova with Holm-Sidac correction. d-e.) The length (d) of mitochondria belonging to each morphological type in hypha grown at 22°C (graph in 2d.) and 18°C (graph in 2e.) shown as average value and SD in each hypha (18°C group, n=4 and 22°C group, n=3). f.) Average length of elongated mitochondria. T-test with Welch's correction.

Acknowledgment

The authors acknowledge funding provided by the Ministry of Science Technological Development and Innovation, Republic of Serbia through the Grants: No. 451-03-47/2023-01/200007, 451-03-47/2023-01/200178, 451-03-47/2023-01/ 200053; by Science Fund of the Republic of Serbia, grant number 4545 [BioPhysFUN]; by the Institute of Physics Belgrade, through the grant provided by the Ministry of Science Technological Development and Innovation.

References

[1] A.R. Fenton, T.A. Jongens, E.L.F. Holzbaur. *Mitochondrial dynamics: Shaping and remodeling an organelle network.* Curr Opin Cell Biol. 68 (2021) 28-36.

[2] T. Pajic, S. Kozakijevic, A.J. Krmpot, *et al*. *In vivo multiphoton imaging of a filamentous fungus Phycomyces blakesleeanus: the effect of small ambient temperature increase on mitochondrial morphology and lipid droplets density*. IX International School and Conference on Photonics, PHOTONICA 2023, August 28 – September 1, 2023, Belgrade-Serbia.

[3] M. Stanić, J. Zakrzewska, M. Hadžibrahimović, *et al*. *Oxygen regulation of alternative respiration in fungus Phycomyces blakesleeanus: connection with phosphate metabolism*. Res Microbiol. 164(7) (2013) 770-8.

[4] T. Pajić, N.V. Todorović, M. Živić, *et al*. *Label-free third harmonic generation imaging and quantification of lipid droplets in live filamentous fungi*. Sci Rep. 12(1) (2022) 18760.

retains its degree of dispersion for one week. Therefore, this model is a suitable candidate for further research and development of a lipid-based dosage form for Alendronate sodium.

S13-BMP-200 / **Poster presentation**

Determination of spatial resolution of nonlinear laser scanning microscopy

Authors: Aleksa Dencevski[1]; Jovana Jelic[1]; Marta Bukumira[1]; Aleksandar Krmpot[1]; Ana Senkic[2]; Antonio Supina[2]; Mihailo Rabasovic[1]; Natasa Vujicic[2]; Stanko Nikolic[1]

[1] *Institute of Physics Belgrade*

[2] *Institute of Physics Zagreb*

Presenter: M. Bukumira (marta@ipb.ac.rs)

Microscope resolution is the shortest distance between two points on a sample that can be distinguished as separate entities. Due to the wave nature of light and the phenomenon of diffraction, it is fundamentally limited: even under theoretically ideal conditions and optical components, the microscope has a finite resolution.

In this paper, we determined lateral and axial resolution of a nonlinear laser scanning microscope by measuring its point spread function (PSF) in two ways: by imaging fluorescent beads using two-photon excited fluorescence (standard method), and by using monolayers of molybdenum disulfide – MoS_2 (non-standard method), obtained by chemical vapor deposition [1], which, due to the lack of central symmetry, efficiently generate second harmonic signal.

Parameters such as the numerical aperture of the objective and the excitation wavelength contribute to the resolution, so it changes depending on the current setting of the microscopic system. Measurements were performed for two different objectives and several standard excitation wavelengths, depending on the type of sample. As expected, the best resolution was obtained for the objective with the largest numerical aperture (40x 1.3) and the shortest excitation wavelength (730nm): $R_{lat} = 260nm$, $R_{ax} = 1648nm$. In addition, the values obtained by the non-standard method are closer to the theoretical values of the resolution, because the contributions of the out-of-focus signal are significantly smaller due to the two-dimensional nature of the layers. This implies that it is better to use this type of sample to determine the resolution of the microscope. The measured PSF can be further used to deconvolve the images obtained on this microscope.

Due to its properties such as large penetration depth of incident radiation and label-free imaging, as well as the possibility of obtaining 3D models, our microscope is widely used in examination of the samples of biological origin, such as: erythrocytes [2], chitinous structures [3], human colon tissue [4], collagen and dentin.

Acknowledgements: The work was funded by the Science Fund of the Republic of Serbia, within PROMIS program, through HEMMAGINERO project and by the Institute of Physics Belgrade, through the grant by the Ministry of Education, Science and Technological Development of the Republic of Serbia.. The authors would like to thank prof. Vladana Vukojevic from Karolinska Institute in Stockholm, Sweden for providing fluorescent beads.

References

1. A. Senkic *et al.*, in preparation, CVD growth parameters on global and local optical properties of MoS2 monolayer
2. K. Bukara *et al.*, J. Biomed. Opt. **22**(2), 026003 (2017)
3. MD Rabasovic *et al.*, J. Biomed. Opt. **20**(1), 016010 (2015)
4. SZ Despotovic *et al.*, Sci. Rep. **10**, 6359 (2020)

S13-BMP-201 / **Poster presentation (virtual)**

Calorimetric Tracking of the Plasma and CSF Proteome in Children With Acute Lymphoblastic Leukemia

Authors: B. Antonova[1]; K. Batchvarov[2]; Yoan Dimitrov[1]; S. Abarova[1]; B. Tenchov[1]; B. Avramova[2]; M. Jordanova[2]; D. Konstantinov[2]

[1] *Medical Faculty, Medical University – Sofia, Bulgaria*

[2] *Department of Pediatric Hematology and Oncology, University Hospital "Queen Joanna", Sofia, Bulgaria*

Presenter: Y. Dimitrov (yoandimitroff@gmail.com)

Leukemia is the most common type of cancer found in children. It accounts for around 33% of all malignant diseases in pediatrics.

Differential scanning calorimetry DSC is a highly sensitive technique that measures temperature-induced conformation changes in proteins. As such, it is useful in measuring the exact values of concentration, conformation and interaction between proteins and other molecules and allows for observing specific insignificant changes in blood plasma and CSF (cerebrospinal fluid), related to various pathological processes. This way, plasma and CSF proteins could serve as biomarkers for the diagnosis and monitoring of the disease.

In this study we have used DSC to compare alterations in the protein thermal denaturation profiles of blood plasma and CSF, taken from children with acute lymphoblastic leukemia (ALL), with the corresponding fluids from other children in continuous remission with healthy clinical and hematological statuses, used as controls.

Here we present DSC measurements of blood plasma in children in cases with leukemic infiltration present in the bone marrow. In some cases they are about newly developed disease or relapsed one, and in other cases about Non-Hodgkin's lymphoma with secondary spread to the bone marrow and also lymphoid blast crisis

Cutting edge technique for determination of spatial resolution limits of nonlinear laser scanning microscopy

M. Bukumira[1], J. Jelić[1], A. Denčevski[1], M.D. Rabasović[1], N. Vujičić[2], A. Senkić[2], A. Supina[2] and A. Krmpot[1]

[1]*Institute of Physics Belgrade, University of Belgrade, Laboratory for Biophysics, Belgrade, Serbia*
[2]*Institute of Physics, Center of Exellence for advanced Materials and Sensing devices, Zagreb, Croatia*
e-mail: marta@ipb.ac.rs

Microscope resolution is the shortest distance between two points on a sample that can be distinguished as separate entities. Due to the wave nature of light and the phenomenon of diffraction, it is fundamentally limited: even under theoretically ideal conditions and optical components, the microscope has a finite resolution.
In this paper, we determined the lateral and axial resolution of a nonlinear laser scanning microscope by measuring its Point Spread Function (PSF). The measurement was preformed in two ways: by imaging fluorescent beads using two-photon excited fluorescence (standard method), and by using transition metal dichalcogenide monolayers of molybdenum disulfide and tungsten disulfide (cutting edge method). The monolayers - obtained by chemical vapor deposition [1], efficiently generate second harmonic (SHG) signal due to the lack of central symmetry. The monolayers were also used for determination of the lateral resolution of third harmonic generation (THG) microscopy.
Measurements were performed for different objectives and several standard excitation wavelengths, depending on the type of sample. As expected, the best resolution was obtained for the objective with the largest numerical aperture and the shortest excitation wavelength. In addition, the values obtained by the non-standard cutting edge method are closer to the theoretical values of the resolution, because the contributions of the out-of-focus signal are significantly reduced due to the two-dimensional nature of the layers. The measured PSF can be further used to deconvolve the images obtained on this microscope.
Due to its properties such as great depth of penetration of incident radiation and label-free imaging, as well as the possibility of making 3D models, our microscope is widely used in examining samples of biological origin, such as: erythrocytes [2], chitin structures [3], human colon [4], collagen, dentin, etc.

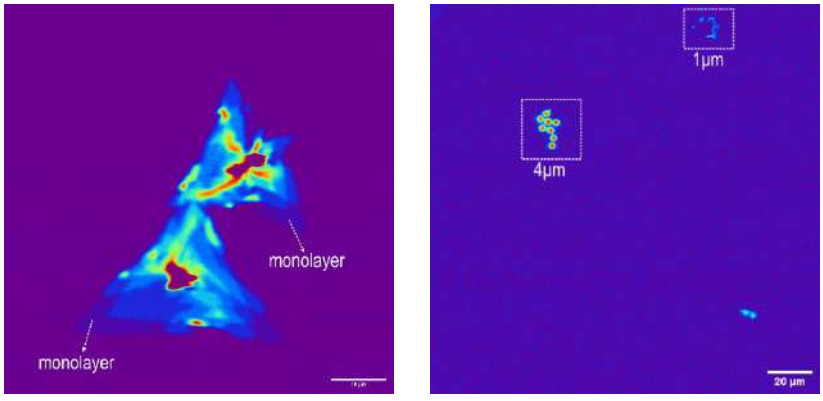

Figure 1. Left: WS_2 (mono)layers; right: fluorescent beads of different diameters (4µm and 1µm).

REFERENCES
[1] A. Senkic *et al.*, Mater. Chem. Phys. 296, 127185 (2023).
[2] K. Bukara *et al.*, J. Biomed. Opt. 22, 026003 (2017).
[3] M.D. Rabasovic *et al.*, J. Biomed. Opt. 20, 016010 (2015).
[4] S.Z. Despotovic *et al.*, Sci. Rep. 10, 6359 (2020).

Contribution submission to the conference Berlin 2024

Insights from live non-linear microscopy imaging: comparative analysis of temperature-induced mitochondrial morphology shifts using standard versus machine-learning method —
•Marta Bukumira[1], Aleksandra Vitkovac[2], Tanja Pajić[2], Marina Stanić[3], Mihailo Rabasović[1], and Nataša V. Todorović[4] — [1]University of Belgrade, Institute of Physics, Belgrade, Serbia — [2]University of Belgrade, Faculty of Biology, Belgrade, Serbia — [3]University of Belgrade, Institute for Multidisciplinary Research, Belgrade, Serbia — [4]University of Belgrade, Institute for Biological Research "Siniša Stanković", Belgrade, Serbia

Using two-photon excited fluorescence (TPEF) modality of our home built nonlinear laser scanning microscope, we investigated, as a proof of principle, mitochondrial morphology adaptations in an eukaryotic cell in vivo, as a response to cooler ambient temperature during growth. The cells were stained with the vital mitochondrial dye Rhodamine 123 in order for mitochondria to exhibit TPEF. We compared cultures grown at two cooler and one control temperature. Acquired images show superior level of clarity and an optimal signal-to-noise ratio, allowing for the morphology differentiations of intricate subcellular structures influenced by subtle temperature variations. Two approaches for extracting parameters from TPEF images were juxtaposed: standard method of particle analysis in ImageJ and nonstandard method in Ilastik, a machine learning-based software. The latter demonstrated greater suitability for this type of analysis, showing increased efficiency in terms of time and reduced susceptibility to errors.

Part: BP
Type: Poster
Topic: Bioimaging
Keywords: TPEF; Imaging; Machine-learning; Mitochondria
Email: marta@ipb.ac.rs

P16

One-Step Synthesis of Biocompatible $NaY_{0.65}Gd_{0.15}F_4$:Yb,Er Upconverting Nanoparticles for *In Vitro* Cell Imaging

Nina Tomić[1], Ivana Dinić[1], Marina Vuković[2], Marta Bukumira[3], Mihailo Rabasović[3], Lidija Mančić[1]

[1]Institute of Technical Science of SASA, KnezaMihaila 35/4, Belgrade, Serbia
[2]Innovative Centre, Faculty of Chemistry, University of Belgrade, Serbia
[3] Photonic Center, Institute of Physics, Belgrade, University of Belgrade, Serbia

There is a great technological interest in synthesis of lanthanide doped upconverting nanoparticles (UCNPs) with controlled crystal phase, morphology and intense luminescence properties suitable for biomedical use. A conventional approach for synthesis of such particles comprises decomposition of organometallic compounds in an oxygen-free environment, followed either with a ligand exchange, or biocompatible layer coating. Biocompatible $NaY_{0.65}Gd_{0.15}F_4$:Yb,Er nanoparticles used in this study were synthesized through chitosan assisted one-pot hydrothermal synthesis and were characterized by X-ray powder diffraction (XRPD), Fourier-transform infrared (FTIR) spectroscopy, scanning electron microscopy coupled with energy dispersive X-ray spectroscopy (SEM/EDS) and photoluminescence measurement (PL). Due to the presence of the amino groups at their surface, excellent biocompatibility and notably low cytotoxicity against MRC-5 cells (line of normal human fibroblasts) and A549 cells (human lung cancer cells) were detected using MTT assay. Furthermore, upon 980 nm laser irradiation, particles were successfully used *in vitro* for labeling of both, MRC-5 and A549 cells.

P17

Characterization of NTC thick film thermistor paste $Cu_{0.2}Ni_{0.5}Zn_{1.0}Mn_{1.3}O_4$

Stanko O. Aleksić[1], Nina N. Obradović[2], Nebojša S. Mitrović[1], Miloljub D. Luković[3]

[1]Faculty of Technical Sciences, Čačak, Svetog Save 65, Čačak 32000, University of Kragujevac, Serbia
[2]Institute of Technical Sciences, SASA, Kneza Mihaila 35, Belgrade 11000, Serbia
[3]Information Technology School-ITS, Cara Dušana 34, Zemun 11080, Serbia

A powder of $Cu_{0.2}Ni_{0.5}Zn_{1.0}$ $Mn_{1.3}O_4$ composition for custom thermistor was prepared by using a certain mixture of metal oxides and solid state reaction at 1000 °C/4h in air. The obtained thermistor powder was milled in the planetary ball mill and agate mill for a prolonged time to achieve submicron powder. The prepared thermistor powder was further characterized by using XRD and SEM techniques. After that, the thermistor powder was pressed into small disc-shaped samples and sintered at 1150 °C/2h. The sintered samples were also characterized by using XRD and SEM. The main electrical properties such as nominal resistance R and thermistor exponential factor B were measured in the climatic test chamber. After that, the thick film paste was prepared using the same powder, an organic vehicle and a glass frit. The paste was printed on alumina substrate, dried at 150 °C / 30 min and sintered in